



**HAL**  
open science

## The MUSE Hubble Ultra Deep Field Survey

Nicolas F. Bouché, Shy Genel, Alisson Pellissier, Cédric Dubois, Thierry Contini, Benoît Epinat, Annalisa Pillepich, Davor Krajnović, Dylan Nelson, Valentina Abril-Melgarejo, et al.

► **To cite this version:**

Nicolas F. Bouché, Shy Genel, Alisson Pellissier, Cédric Dubois, Thierry Contini, et al.. The MUSE Hubble Ultra Deep Field Survey: XVI. The angular momentum of low-mass star-forming galaxies: A cautionary tale and insights from TNG50. *Astronomy and Astrophysics - A&A*, 2021, 654, pp.A49. 10.1051/0004-6361/202040225 . hal-03371795

**HAL Id: hal-03371795**

**<https://hal.science/hal-03371795>**


Submitted on 8 Oct 2021

**HAL** is a multi-disciplinary open access archive for the deposit and dissemination of scientific research documents, whether they are published or not. The documents may come from teaching and research institutions in France or abroad, or from public or private research centers.

L'archive ouverte pluridisciplinaire **HAL**, est destinée au dépôt et à la diffusion de documents scientifiques de niveau recherche, publiés ou non, émanant des établissements d'enseignement et de recherche français ou étrangers, des laboratoires publics ou privés.

## The MUSE *Hubble* Ultra Deep Field Survey

### XVI. The angular momentum of low-mass star-forming galaxies: A cautionary tale and insights from TNG50

Nicolas F. Bouché<sup>1</sup> , Shy Genel<sup>2,3</sup>, Alisson Pellissier<sup>4,5</sup>, Cédric Dubois<sup>4</sup>, Thierry Contini<sup>4</sup>, Benoît Epinat<sup>6</sup>, Annalisa Pillepich<sup>7</sup>, Davor Krajnović<sup>8</sup>, Dylan Nelson<sup>9</sup>, Valentina Abril-Melgarejo<sup>6</sup>, Johan Richard<sup>1</sup>, Leindert Boogaard<sup>7,10</sup>, Michael Maseda<sup>10,12</sup>, Wilfried Mercier<sup>4</sup>, Roland Bacon<sup>1</sup>, Matthias Steinmetz<sup>8</sup>, and Mark Vogelsberger<sup>11</sup>

<sup>1</sup> Univ Lyon, Univ Lyon1, ENS de Lyon, CNRS, Centre de Recherche Astrophysique de Lyon (CRAL) UMR5574, 69230 Saint-Genis-Laval, France

e-mail: nicolas.bouche@univ-lyon1.fr

<sup>2</sup> Center for Computational Astrophysics, Flatiron Institute, 162 Fifth Avenue, New York, NY 10010, USA

<sup>3</sup> Columbia Astrophysics Laboratory, Columbia University, 550 West 120th Street, New York, NY 10027, USA

<sup>4</sup> Institut de Recherche en Astrophysique et Planétologie (IRAP), Université de Toulouse, CNRS, UPS, 31400 Toulouse, France

<sup>5</sup> Laboratoire Lagrange, Université Côte d'Azur, Observatoire de la Côte d'Azur, CNRS, Blvd de l'Observatoire, 06304 Nice cedex 4, France

<sup>6</sup> Aix Marseille Univ, CNRS, CNES, LAM, Marseille, France

<sup>7</sup> Max-Planck-Institut für Astronomie, Königstuhl 17, 69117 Heidelberg, Germany

<sup>8</sup> Leibniz-Institut für Astrophysik Potsdam (AIP), An der Sternwarte 16, 14482 Postdam, Germany

<sup>9</sup> Universität Heidelberg, Zentrum für Astronomie, Institut für theoretische Astrophysik, Albert-Ueberle-Str. 2, 69120 Heidelberg, Germany

<sup>10</sup> Leiden Observatory, Leiden University, PO Box 9513, 2300 RA Leiden, The Netherlands

<sup>11</sup> Department of Physics, Massachusetts Institute of Technology, 77 Massachusetts Avenue, Cambridge, MA 02139, USA

<sup>12</sup> Department of Astronomy, University of Wisconsin-Madison, 475 N. Charter Street, Madison, WI 53706, USA

Received 23 December 2020 / Accepted 19 June 2021

#### ABSTRACT

We investigate the specific angular momentum (sAM)  $j(<r)$  profiles of intermediate redshift ( $0.4 < z < 1.4$ ) star-forming galaxies (SFGs) in the relatively unexplored regime of low masses (down to  $M_* \sim 10^8 M_\odot$ ) and small sizes (down to  $R_e \sim 1.5$  kpc), and we characterize the sAM scaling relation (i.e., Fall relation) and its redshift evolution. We have developed a 3D methodology to constrain sAM profiles of the star-forming gas using a forward modeling approach with GALPAK<sup>3D</sup> that incorporates the effects of beam smearing, yielding the intrinsic morpho-kinematic properties even with limited spatial resolution data. Using mock observations from the TNG50 simulation, we find that our 3D methodology robustly recovers the star formation rate (SFR)-weighted  $\tilde{j}_*(<r)$  profiles down to a low effective signal-to-noise ratio of  $\gtrsim 3$ . We applied our methodology blindly to a sample of 494 [O II]-selected SFGs in the MUSE Ultra Deep Field (UDF) 9 arcmin<sup>2</sup> mosaic data, covering the unexplored  $8 < \log M_*/M_\odot < 9$  mass range. We find that the (SFR-weighted) sAM relation follows  $\tilde{j}_* \propto M_*^\alpha$  with an index  $\alpha$  varying from  $\alpha = 0.3$  to  $\alpha = 0.5$ , from  $\log M_*/M_\odot = 8$  to  $\log M_*/M_\odot = 10.5$ . The UDF sample supports a redshift evolution  $\tilde{j}_* \propto (1+z)^a$ , with  $a = -0.27^{+0.42}_{-0.56}$  which is consistent with the  $(1+z)^{-0.5}$  expectation from a universe in expansion. The scatter of the sAM sequence is a strong function of the dynamical state with  $\log j|_{M_*} \propto 0.65^{+0.06}_{-0.08} \times \log(V_{\max}/\sigma)$ , where  $\sigma$  is the velocity dispersion at  $2R_e$ . In TNG50, SFGs also form a  $\tilde{j}_* - M_* - (V/\sigma)$  plane, but it correlates more with galaxy size than with morphological parameters. Our results suggest that SFGs might experience a dynamical transformation, and lose their sAM, before their morphological transformation to becoming passive via either merging or secular evolution.

**Key words.** galaxies: high-redshift – galaxies: evolution – galaxies: kinematics and dynamics – galaxies: structure

#### 1. Introduction

In a  $\Lambda$  cold dark matter (ACDM) universe, baryons cool, fall inwards, and form centrifugally supported disks in the centers of halos. The specific angular momentum (sAM) sets the pressure, instabilities, gas fractions (Obreschkow et al. 2016; Romeo & Mogotsi 2018; Romeo 2020; Li et al. 2020), and most importantly determines the disk properties, such as size (e.g., White & Rees 1978; Fall & Efstathiou 1980; Fall 1983; Mo et al. 1998; Dalcanton et al. 1997; van den Bosch et al. 2003; Dutton & van den Bosch 2009; Somerville et al. 2018). As disks

evolve from  $z = 2$  to the present, they must grow from a vast reservoir of corotating cold accreting material in the circumgalactic medium (CGM) as argued in Renzini (2020). This is also strongly supported by hydro-dynamical simulations which predict roughly coplanar gaseous structures (Stewart et al. 2013, 2017; Danovich et al. 2015; Ho et al. 2019; Kretschmer et al. 2020; DeFelippis et al. 2021) embedded in a rotating CGM (DeFelippis et al. 2020). These coplanar structures were initially found by Barcons et al. (1995) and Steidel et al. (2002) in a handful of background quasar sight-lines, but they are now routinely observed on scales of 20–80 kpc (as in Bouché et al. 2013, 2016;

Ho et al. 2017; Lopez et al. 2018; Martin et al. 2019; Zabl et al. 2019). These structures are important as they not only bring fuel for star-formation but also angular momentum (Renzini 2020; DeFelippis et al. 2021).

In this context, one of the most fundamental properties of disk galaxies is their sAM (as argued in Fall & Efstathiou 1980). The sAM of halos ( $j_h = J_h/M_h$ ) is tightly correlated to the halo mass  $M_h$  ( $j_h \propto M_h^{2/3}$ ) as a result of tidal torques from the large-scale structure (e.g., Peebles 1969; Efstathiou & Jones 1979). It is often assumed that the sAM of baryons and of dark matter are equal at accretion, and that as disks form in the centers of halos the baryonic sAM is conserved (e.g., Fall & Efstathiou 1980; Mo et al. 1998; Burkert et al. 2010). While this assumption of  $j$  conservation during collapse has been appealing since the late 1970s (e.g., White & Rees 1978; Fall & Efstathiou 1980), it is not trivial given the infalling baryons can both lose and gain angular momentum from the virial radius to the inner disk (e.g., Navarro & Steinmetz 2000; Sharma et al. 2012; Danovich et al. 2015; Genel et al. 2015; DeFelippis et al. 2017; Jiang et al. 2019). In particular, Genel et al. (2015) and DeFelippis et al. (2017) found that galactic winds are essential for producing late-type galaxies with sufficient angular momentum.

Observationally, the stellar sAM of massive disks (with  $\log M_\star/M_\odot > 9$ ) follows a similar scaling relation as the dark matter  $j_h - M_h$  scaling relation with  $j_\star \propto M_\star^\alpha$  with  $\alpha \approx 0.6$ , as reported by M. Fall and collaborators (Fall 1983; Romanowsky & Fall 2012; Fall & Romanowsky 2013, hereafter FR13) and recently revisited by Fall & Romanowsky (2018, hereafter FR18). This similarity between the halo and baryonic sAM scaling relations, both in normalization (for galaxy disks) and slope, highlights a potential intimate link between galaxies and their host DM haloes, as discussed extensively in Posti et al. (2018b). However, hydrodynamical simulations tend to show a more complex relation between the DM and baryonic sAM (e.g., Genel et al. 2015; Jiang et al. 2019).

Since the pioneering study of Fall (1983), the  $j_\star - M_\star$  relation has become a standard tool in galaxy evolution research thanks to recent Integral Field Spectrograph (IFS) surveys and to more accurate simulations of disk formation (e.g., Vogelsberger et al. 2012, 2013; Schaye et al. 2015; Ceverino et al. 2017; Grand et al. 2019; Nelson et al. 2019; Pillepich et al. 2019), see review in Vogelsberger et al. (2020). Hence, understanding the slope and normalization of this important scaling relation is of paramount importance as it is intimately related to galaxy morphological diversity and holds clues to accretion of baryons onto galaxies (Genel et al. 2015; Teklu et al. 2015; Zavala et al. 2016; Lagos et al. 2017; El-Badry et al. 2018).

In the local universe, several groups have expanded on the work of Fall and collaborators to confirm the  $j_\star - M_\star$  relation with increasingly large samples of galaxies as in Cortese et al. (2016) and Lapi et al. (2018) which each had  $\sim 500$  galaxies, albeit mostly with  $M_\star > 10^{9.5} M_\odot$ . Some of these local surveys have shown that the scatter of the  $j_\star - M_\star$  relation strongly correlates with morphology (Obreschkow & Glazebrook 2014; Cortese et al. 2016; Rizzo et al. 2018; Sweet et al. 2018). At lower masses  $M_\star < 10^9 M_\odot$ , the  $j_\star - M_\star$  relation is not understood as well either theoretically (e.g., Stevens et al. 2016; Mitchell et al. 2018; El-Badry et al. 2018) or observationally (but see Butler et al. 2017; Posti et al. 2018a; Mancera Piña et al. 2021). Both the sample of 14 dIrr galaxies in the  $10^6 - 10^9 M_\odot$  mass range from Butler et al. (2017) and the local disks with  $M_\star > 10^7 M_\odot$  from Posti et al. (2018a) and Mancera Piña et al. (2021) show that the  $j_\star - M_\star$  relation is well described by a single power-law at all scales with a slope  $\alpha = 0.6 \pm 0.1$  (see Fall & Romanowsky 2018).

At high redshifts, studying the  $j - M$  relation has become particularly important in order to constrain the redshift evolution of this fundamental scaling relation. Thanks to recent advancements with second generation IFS instruments, such as the Multi-Unit Spectroscopic Explorer (MUSE; Bacon et al. 2010) and the  $K$ -band Multi-Object Spectrograph (KMOS; Sharples et al. 2013), several groups have constrained the  $j - M$  relation using increasingly larger samples of  $z > 1$  star-forming galaxies (SFGs). Among these, there is the sample of 360 SFGs from the SINS/KMOS3D survey (Burkert et al. 2010, 2016; Wisnioski et al. 2019) at redshifts  $0.8 < z < 2.3$ , the sample of  $\approx 400$  SFGs at  $z \sim 0.8$  of Swinbank et al. (2017) collected in MUSE and KMOS surveys, and the sample of 486  $z = 0.6 - 1.0$  SFGs (Harrison et al. 2017) from the KROSS  $H\alpha$  survey (Stott et al. 2016). These surveys (and others, e.g. Alcorn et al. 2018; Gillman et al. 2020) are often limited to relatively massive SFGs with a typical limit of  $M_\star > 10^{9.5} M_\odot$ .

The  $j - M$  relation has also not been explored in the low mass regime at  $M_\star$  of  $10^8 M_\odot - 10^{9.5} M_\odot$  beyond the local universe (Posti et al. 2018a). Thanks to the MUSE IFS (Bacon et al. 2010) and its exquisite sensitivity, it is now possible to study the kinematics of SFGs at low masses down to  $M_\star = 10^8 M_\odot$ , as first demonstrated by Contini et al. (2016). The low-mass regime ( $M_\star = 10^{8-9} M_\odot$ ) is challenging as galaxies become marginally resolved (when smaller than 3 kpc), and it becomes difficult to recover reliable measurements of both sizes and rotation velocity.

This paper aims to show that the  $j - M$  relation can be characterized in small and low-mass galaxies at redshifts from  $z = 0.4 - 1.4$ , opening up new parameter space thanks to the MUSE instrument and to our 3D modeling approach. Contrary to galaxies in the local universe where the  $j - M$  relation can be studied independently for the stellar  $j_\star$  or gas components  $j_{\text{gas}}$  (e.g., Obreschkow & Glazebrook 2014; Obreschkow et al. 2016; Li et al. 2020; Mancera Piña et al. 2021), this is currently extremely challenging in distant galaxies at  $z \approx 1.0$  or beyond. One should note that the gas sAM  $j_{\text{gas}}$  in this context is derived solely from HI data at  $z = 0$ , and it is often assumed that the sAM for the star-forming gas (molecular or ionized) is similar to  $j_\star$  because of the similar extent (Leroy et al. 2008; Nelson et al. 2016; Wilman et al. 2020) and kinematics (Martinsson et al. 2013; Lang et al. 2020)<sup>1</sup>. As discussed in the next section, we focus our analysis on the sAM  $j$  derived from the star-forming gas, denoted  $\tilde{j}_\star$ , both for a large sample of 494 SFGs from the MUSE *Hubble* Ultra Deep Field (UDF) observations presented in Bacon et al. (2017) and for SFGs from the TNG50 simulations (Nelson et al. 2019; Pillepich et al. 2019).

This paper is organized as follows. In Sect. 2, we present our methodology that is designed to be more accurate in the low-mass regime. In Sect. 3, we validate our methodology on 158 simulated galaxies taken from TNG50. In Sect. 4, we apply our methodology on 494 galaxies in the MUSE UDF. In Sect. 5, we compare our results to  $\sim 5000$  SFGs in TNG50. We discuss the implication of our results in Sect. 6. Finally, we present our conclusions in Sect. 7. Throughout this paper, we use a ‘‘Planck 2015’’ cosmology (Planck Collaboration XIII 2016) with  $\Omega_M = 0.307$ ,  $\Lambda = 0.693$ ,  $H_0 = 67 \text{ km s}^{-1} \text{ Mpc}^{-1}$ , yielding  $8.23 \text{ kpc arcsec}^{-1}$ , and we consistently use ‘‘log’’ for the base-10 logarithm.

<sup>1</sup> See Marasco et al. (2019) for details on the conversion between  $j_{\text{gas}}$  and  $j_\star$ .

## 2. Measuring angular momentum

### 2.1. Definitions

The sAM  $j \equiv J/M$  is, in general, given by

$$j_{\text{tot}} \equiv \frac{J}{M} = \frac{\int \rho(\mathbf{x})(\mathbf{v} \times \mathbf{x})d^3\mathbf{x}}{\int \rho(\mathbf{x})d^3\mathbf{x}}. \quad (1)$$

In practice, the two-dimensional version of the specific angular momentum, appropriate for an axi-symmetric disk, is used

$$j(<R) = j_{2d}(<R) = \frac{\int_0^R \Sigma(r)v(r)r^2 dr}{\int_0^R \Sigma(r)r dr}, \quad (2)$$

where  $R$  is the enclosed radius,  $\Sigma(r)$  the surface brightness, and  $v(r)$  the rotation velocity profile.

Regarding Eq. (2), the total angular momentum  $j_{\text{tot}} \equiv j(<\infty)$  is not observable directly as inherent surface brightness limitations preclude measurements beyond  $R_e$  or at best  $2R_e$  (e.g., Marasco et al. 2019). For massive galaxies, probing  $j$  up to  $R_e$  or  $2R_e$ , where the  $j$  profile reaches its plateau, might be sufficient, but in low mass galaxies, that regime might be difficult to reach even in the local universe, as discussed in Posti et al. (2018a), Marasco et al. (2019). Thus, previous work often resorted to estimators for  $j_{\text{tot}}$  such as Eq. (3), which is discussed in Sect. 2.2. Here, we use a 3D methodology (Sect. 2.3) that bypasses common approximations and similar in essence to the analysis of Mancera Piña et al. (2021) who used <sup>3D</sup>Barolo (Di Teodoro & Fraternali 2015). In Sect. 3, we show with mock cubes from TNG50 that our 3D method combined with Eq. (2) does reproduce the true  $j$  values, computed directly from Eq. (1).

It is worth noting that in order to determine  $j_*(r)$  from Eq. (2), one needs the stellar mass profile  $\Sigma_*(r)$  and the stellar rotation curve  $v_*(r)$ . However, determining stellar kinematics beyond  $z = 0$  is challenging in SFGs (but see Guérou et al. 2017, for a first attempt) or even in passive galaxies with strong continuum (e.g., van de Sande et al. 2013; Bezanson et al. 2018; Cole et al. 2020). As a result, most studies of the  $j_* - M_*$  relation use the star-forming gas  $v_{\text{H}\alpha}$  kinematics as a proxy for  $v_*$  (e.g., Burkert et al. 2016; Harrison et al. 2017; Swinbank et al. 2017). Two studies attempted to convert  $v_{\text{H}\alpha}$  to  $v_*$ , Marasco et al. (2019) at  $z = 1$  and Posti et al. (2018a) at  $z = 0$  using the asymmetric drift correction (Meurer et al. 1996; Dalcanton & Stilp 2010; Burkert et al. 2010).

Regarding the stellar mass profile  $\Sigma_*(r)$ , it acts as the normalization factor in Eq. (2), and thus one only need to know the profile shape, namely the Sérsic index and the half-light radius  $R_e$ . For SFGs, one can use the star-forming gas profile  $\Sigma_{\text{H}\alpha}$  (or  $\Sigma_{[\text{O II}]}$ ) as a proxy for  $\Sigma_*$  provided that the SF gas and stars have similar scale length<sup>2</sup>, which is expected from the almost linear Kennicutt-Schmidt relation (Kennicutt 1998; Genzel et al. 2010; Daddi et al. 2010; Bacchini et al. 2019). In fact, the  $\text{H}\alpha$  size  $R_{e,\text{H}\alpha}$  to continuum size ratio  $R_{e,*}$  has been found to be  $\approx 1^3$  from a very large sample of 3200 galaxies at  $0.7 < z < 1.5$  with WFC3 imaging in Nelson et al. (2016), confirmed in our data as discussed in Sect. 4.2.

In this paper, we measure the star formation rate (SFR)-weighted sAM  $j_{\text{sfr}}$  determined from the star-forming gas properties, namely  $v_{[\text{O II}]}(r)$  and  $\Sigma_{[\text{O II}]}(r)$ , as a proxy for  $j_*$  following other studies (e.g., Burkert et al. 2016; Contini et al.

2016; Swinbank et al. 2017). This has the advantage that the measurement is self-contained (from  $\text{H}\alpha$  or  $[\text{O II}]$ ) and that a comparison to similar quantities from simulations can be performed. We use the notation  $\tilde{j}_*$  to designate  $j_{\text{sfr}}$  and in Sect. 3.4, we quantify the potential bias between  $\tilde{j}_*$  and  $j_*$  in the TNG50 galaxies.

### 2.2. 2D Methodology: An Approximate sAM

Given the difficulties in measuring  $j(<r)$  in the outskirts of galaxies, a method that is commonly used in the literature (e.g., Burkert et al. 2016; Swinbank et al. 2017; Harrison et al. 2017; Gillman et al. 2020) for estimating  $j_{\text{tot}}$  is the following formulae (Romanowsky & Fall 2012, hereafter RF12):

$$j_{\text{tot,RF}} = k_n v_s R_e, \quad (3)$$

where  $R_e$  is the half-light radius,  $v_s$  the rotation velocity at  $2R_e$ ,  $v(2R_e)$ , and  $k_n = 1.15 + 0.029 \cdot n + 0.062 \cdot n^2$  is a constant that depends on the Sérsic (1963) index  $n$ . Equation (3) reduces to the well-known  $j_{\text{tot,RF}} = 2 v_s R_d$  for disks with  $R_d$  being the exponential scale length.

However, we caution the reader against using Eq. (3) for low mass galaxies with  $\log(M_*/M_\odot) < 9.5-10$ , for the following reasons. Equation (3) assumes that the velocity profile  $v(r)$  is a constant from  $r = 0$ , which might be appropriate for galaxies with  $\log(M/M_*) > 10$ , but is less suitable for intermediate and low mass galaxies, which are known to have slowly rising rotation curves (e.g., Persic et al. 1996; Catinella et al. 2006). Consequently, Eq. (3) can lead to an over-estimation of the total angular momentum as discussed in Obreschkow & Glazebrook (2014).

To quantify the overestimation in the low-mass regime, we show in Fig. 1(left) several sAM profiles (solid lines), corresponding to ‘‘tanh’’ rotation curves,  $v(r) = V_{\text{max}} \tanh(r/R_t)$  with varying inner slopes (parameterized by the turn-over radius  $R_t$ ), normalized to the RF12 approximation (represented by the blue horizontal line). This figure shows that, for galaxies with slowly rising rotation curves, that is with  $R_t/R_e$  of order unity, Eq. (3) results in an overestimation of the angular momentum by up to 15%. Obreschkow & Glazebrook (2014) made a similar point using rotation curves  $v(r) \propto (1 - \exp(-r/R_t))$ .

Moreover, there can be significant differences between the often used  $k_n$  approximation, namely  $k_n = 1.15 + 0.029 \cdot n + 0.062 \cdot n^2$  and the exact expression (derived in Appendix A) given by:

$$k_n = \left(\frac{1}{b_n}\right)^{1/n} \frac{\Gamma(3n)}{\Gamma(2n)} \quad (4)$$

that can be as large as 15% for Sérsic indices  $n \lesssim 1$  as indicated in Fig. 1(right).

In conclusion, combining these two effects, Eqs. (3) and (4), can lead to an overestimation of the sAM (up to 20–25%) for galaxies with  $n \lesssim 1$  and/or when the rotation curve is slowly rising, that is in the low-mass regime at  $M_* < 10^{9.5} M_\odot$ . In addition, such galaxies with a large turn-over radius  $R_t$  tend to have large sizes and hence a low surface brightness, and thus their true  $V_{\text{max}}$  is more difficult to measure beyond  $R_t$ .

### 2.3. 3D Methodology

In order to estimate  $j$  directly from Eq. (2), one needs the intrinsic (deprojected and free from instrumental and resolution effects) velocity and surface brightness flux profile and these can be measured directly from 3D (position-position-velocity)

<sup>2</sup> This implicitly assumes a small or negligible bulge component.

<sup>3</sup> This ratio is slightly mass-dependent beyond  $10^{10} M_\odot$  reaching 1.2–1.3 at  $10^{11} M_\odot$  in the KMOS3D survey (Wilman et al. 2020).

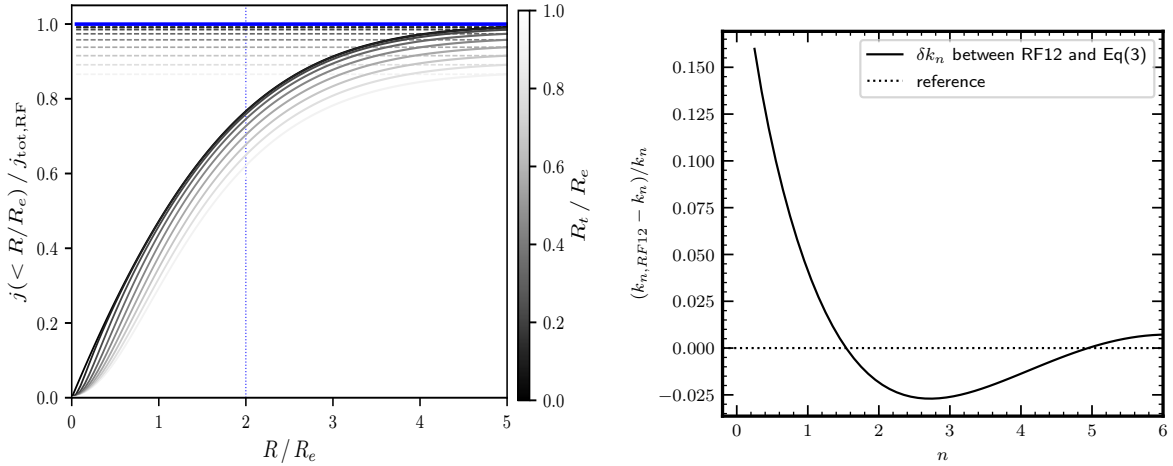


**Fig. 1.** Systematics at play in measuring  $j(<r)$ . *Left:* sAM profile  $j(<r)$  normalized by the RF12 approximation (Eq. (3)) as a function of radius for disks with Sérsic  $n = 1$  and a tanh rotation curve. The solid blue horizontal line represents the Eq. (3) approximation. The solid curves represent the sAM for various rotation curves with various turn-over radii  $R_t$  where the opacity of the line is inversely proportional to  $R_t/R_e$ . The vertical dotted line represents  $2R_e$ . For galaxies with slowly rising rotation curves, with larger  $R_t$ , the RF12 approximation leads to a large overestimation of the total angular momentum (represented by the horizontal dashed lines), by 10–20%. *Right:* relative difference for the  $k_n$  coefficient between the  $k_n$  formula from RF12 and Eq. (4) as a function of Sérsic index  $n$ . One sees that Eq. (3) under- or over-estimate  $k_n$  by up to  $\sim 10\%$  for  $0.5 < n < 4$ .

data using the GAIPAK<sup>3D</sup> algorithm<sup>4</sup> described in Bouché et al. (2015).

Briefly, GAIPAK<sup>3D</sup> performs a parametric fit on emission line data for the morphology and kinematics simultaneously directly onto the 3D data using a 3D  $(x, y, \lambda)$  disk model which specifies the morphology and kinematic profiles. For the morphology, the model assumes a Sérsic (1963) surface brightness profile  $\Sigma(r)$ , with Sérsic index  $n$ . For the kinematics, the model assumes a parametric form for the rotation curve  $v(r)$  and for the dispersion  $\sigma(r)$  profile. The model parameters are the centroid position  $x, y, z$ , the total line flux, the inclination  $i$ , the major-axis position angle P.A., the half-light radius ( $R_e$ ), the turnover radius  $R_t$  and maximum velocity  $V_{\max}$  for the rotation curve, and the velocity dispersion  $\sigma_0$ , described below.

The rotation curve  $v(r)$  can be “arctan”, ‘tanh’ or other analytical forms as described in the documentation<sup>5</sup>. As described in Bouché et al. (2015), the velocity dispersion profile  $\sigma(r)$  is made of three components added in quadrature. The first component  $\sigma_1$  is that of a thick disk (Genzel et al. 2008), namely  $\sigma_1(r)/v(r) = h_z/r$  where  $h_z$  is the disk thickness, taken to be  $0.2 \times R_e$ . The second component  $\sigma_2$  is comes from the natural broadening of the 3D disk model of finite thickness. The third component  $\sigma_3$  is an adjustable constant term  $\sigma_0$ , as in Genzel et al. (2008), Förster Schreiber et al. (2006), Cresci et al. (2009), Wisnioski et al. (2015), Übler et al. (2019) and describes any additional turbulent component to the kinematic dispersions.

GAIPAK<sup>3D</sup> convolves the model with the Point Spread Function (PSF) and the instrumental Line Spread Function (LSF), which implies that the parameters are “intrinsic”, that is corrected for beam smearing and instrumental effects. Here, we use a Moffat PSF as characterized in Bacon et al. (2017), and we use Eq. (7) of Bacon et al. (2017) for the LSF.

GAIPAK<sup>3D</sup> uses a simple Metropolis-Hasting (MH) algorithm to optimize the parameters whose posterior distributions are given by the chain posteriors. As described in Bouché et al. (2015), the GAIPAK<sup>3D</sup> implementation of the MH uses a nonstandard Cauchy proposal distribution which shortens the burn-in phase consider-

ably, but suffers, like most MH algorithms, from the need to manually tune the width of the proposal distribution.

Since its initial release, the following improvements and new features have been implemented in GAIPAK<sup>3D</sup>. First, in order to quantify the chain convergence for each parameter, GAIPAK<sup>3D</sup> performs the Geweke (1992)’s convergence diagnostic test for each of the parameters, which is a Z-test of equality of means (of two parts of the chain) where auto-correlation in the samples is taken into account. Second, GAIPAK<sup>3D</sup> can now adapt the widths of the Cauchy proposal distribution automatically. Third, and most importantly, GAIPAK<sup>3D</sup> is now (since v1.20) compatible with the EMCEE code (Foreman-Mackey et al. 2013). EMCEE has the advantage that its multi-walkers remove the need to tune the proposal distribution, but it has the disadvantage to retain the Normal proposal distribution which is very slow and inefficient in reaching convergence because the Gaussian function does not have broad wings. For our purposes, we combine the self-tuning of our fast MH algorithm implemented in GAIPAK<sup>3D</sup> with the EMCEE sampler once convergence is reached as follows: we first run the self-tuning of our fast MH algorithm with Cauchy sampling, and then use the EMCEE sampler once convergence is reached.

Furthermore, as illustrated in Fig. 2, we use the following two-step process. We first determine the morphological parameters by fitting a 2D Sérsic model to the collapsed [O II] cube (i.e. a two-dimensional flux map), keeping the inclination  $i$  free. This yields estimates of the morphological parameters, namely inclination, size and Sérsic index ( $i_{2d}, R_{e,2d}, n_{2d}$ ). Then, we fit a 3D model with the Sérsic  $n$  fixed to 0.5, 1, 2 or 4 based on  $n_{2d}$ , and tophat priors on the half-light radius  $R_e$  and inclination  $i$  from the results of the 2D analysis (Fig. 2). For the kinematics, we choose a tanh( $r/r_t$ ) rotation curve  $v(r)$  after finding that it gives more robust measurements of  $V_{\max}$  than a arctan profile. Finally, from the morphological and kinematics information, namely  $\Sigma(r)$  and  $v(r)$  we can compute  $j$  using Eq. (2). The total sAM is then calculated from the  $j(<r)$  profile at  $10R_e$ <sup>6</sup>.

<sup>4</sup> Available at <http://galpak3d.univ-lyon1.fr>.

<sup>5</sup> See <http://galpak3d.univ-lyon1.fr/doc/>

<sup>6</sup> Others uses  $j(<R_e)$  (Cortese et al. 2016) or even  $j(<R_{\max})$  where  $R_{\max}$  is the last radius where  $\Sigma_*(r)$  can be measured (e.g., Posti et al. 2018a; Marasco et al. 2019; Mancera Piña et al. 2021), which is prone to biases.

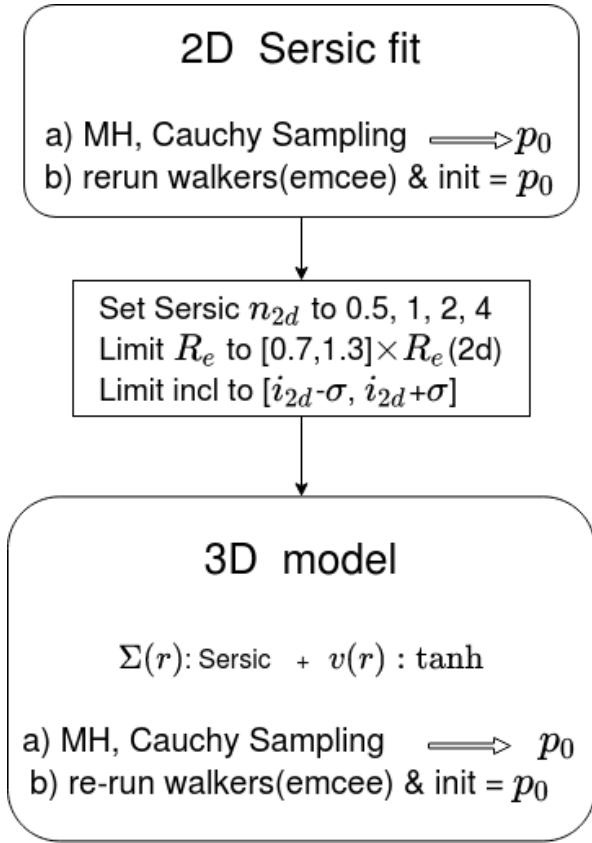


**Fig. 2.** Schematic description of our 3D methodology using a 2-step process. First, we determine the morphological parameters by fitting a 2D Sérsic model for the flux profile  $\Sigma(r)$  on a [O II] image from MUSE. Then, we fit the MUSE [O II] data with 3D model with the Sérsic  $n$  fixed to 0.5, 1, 2 or 4 based on  $n_{2d}$  and priors on the half-light radius  $R_e$  and inclination  $i$  from the results of the 2D analysis. We run the MCMC algorithm in two steps, first with Cauchy sampling which reaches convergence more efficiently, then with EMCEE which better sample the posteriors.

For the velocity dispersion, we evaluate the intrinsic (deconvolved) velocity dispersion profile  $\sigma(r)$  at  $2R_e$ , namely  $\sigma_\tau \equiv \sigma(2R_e)$ . This is a more reliable estimator of the dispersion in the outer regions from our parametrization discussed earlier. Indeed, the fitted parameter,  $\sigma_0$ , can approach zero in some galaxies when the kinematic dispersions ( $\sigma_{1,2}$ ) is sufficient to describe the data. In the remainder of the paper, we use  $\sigma(2R_e)$  as the total velocity dispersion  $\sigma_\tau$  of SFGs.

In summary, our 3D method has several advantages and avoids the shortcomings mentioned in the previous section. In particular, it includes all of the information available by combining the many spaxels with very low signal-to-noise ratio (S/N), down to  $\sim 0.1$  in the outer regions, which are inaccessible with 2D velocity maps. Second, it avoids the assumptions of the Eq. (3) formula, namely of flat rotation curves, which can lead to biases in the low-mass regime. Third, it takes into account the effect of the PSF convolution. And fourth, it is self-consistent and does not rely on external data to break the  $i$ - $V_{\max}$  degeneracy. It does, however, assume that SFGs have regular velocity fields. Our modeling is similar to the DYsmal code used in Bouché et al. (2007), Cresci et al. (2009), Davies et al. (2011), Genzel et al. (2017, 2020), but GALPAK<sup>3D</sup> adjusts the model parameters directly to the raw 3D cube while DYsmal fits the 1D flux, velocity and dispersion maps generated from a 3D model.

### 3. Methodology validation with the TNG50 simulation

As our source of simulated galaxies we employ the TNG50 simulation (Nelson et al. 2019; Pillepich et al. 2019) from the IllustrisTNG project (Springel et al. 2018; Pillepich et al. 2018a; Nelson et al. 2018; Marinacci et al. 2018; Naiman et al. 2018). TNG50 is a cosmological hydrodynamical simulation following a volume of  $(51.7 \text{ Mpc})^3$  at a baryonic (DM) mass resolution of  $8.5 \times 10^4 M_\odot$  ( $4.5 \times 10^5 M_\odot$ ) and a spatial resolution of  $\sim 300 \text{ pc}$ . The simulation is evolved with the AREPO code (Springel 2010), and includes physical models for radiative cooling, star-formation, stellar evolution, black hole growth, as well as feedback channels in the form of galactic winds and several modes of AGN feedback. We refer the reader to Vogelsberger et al. (2013), Weinberger et al. (2017) and Pillepich et al. (2018b) for full details on these models and only describe here the one most directly relevant to this work, namely the star-formation model. Star-formation in TNG50 is based on Springel & Hernquist (2003) and prescribes the star-formation rate as a function of volumetric gas density with a threshold of  $n_{\text{H,th}} = 0.13 \text{ cm}^{-3}$  and a gas consumption timescale of  $2.2 \sqrt{n_{\text{H,th}}/n_{\text{H}}} 1 \text{ Gyr}$ . The TNG simulations reproduce rather well several basic properties of galaxies that are relevant to the topic of this paper, such as galaxy stellar mass functions (Pillepich et al. 2018a) and size-mass relations (Genel et al. 2018) at various redshifts.

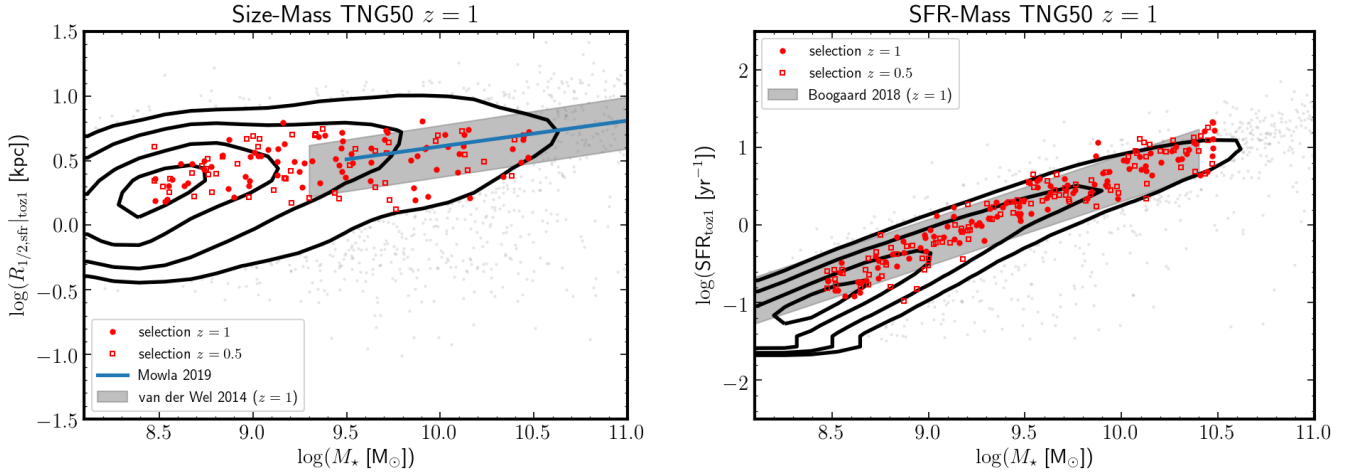
The angular momentum of galaxies was studied by Genel et al. (2015) in the precursor Illustris simulation (Vogelsberger et al. 2014a,b; Genel et al. 2014) and was found to match  $z = 0$  observations within the uncertainties.

#### 3.1. Sample selection

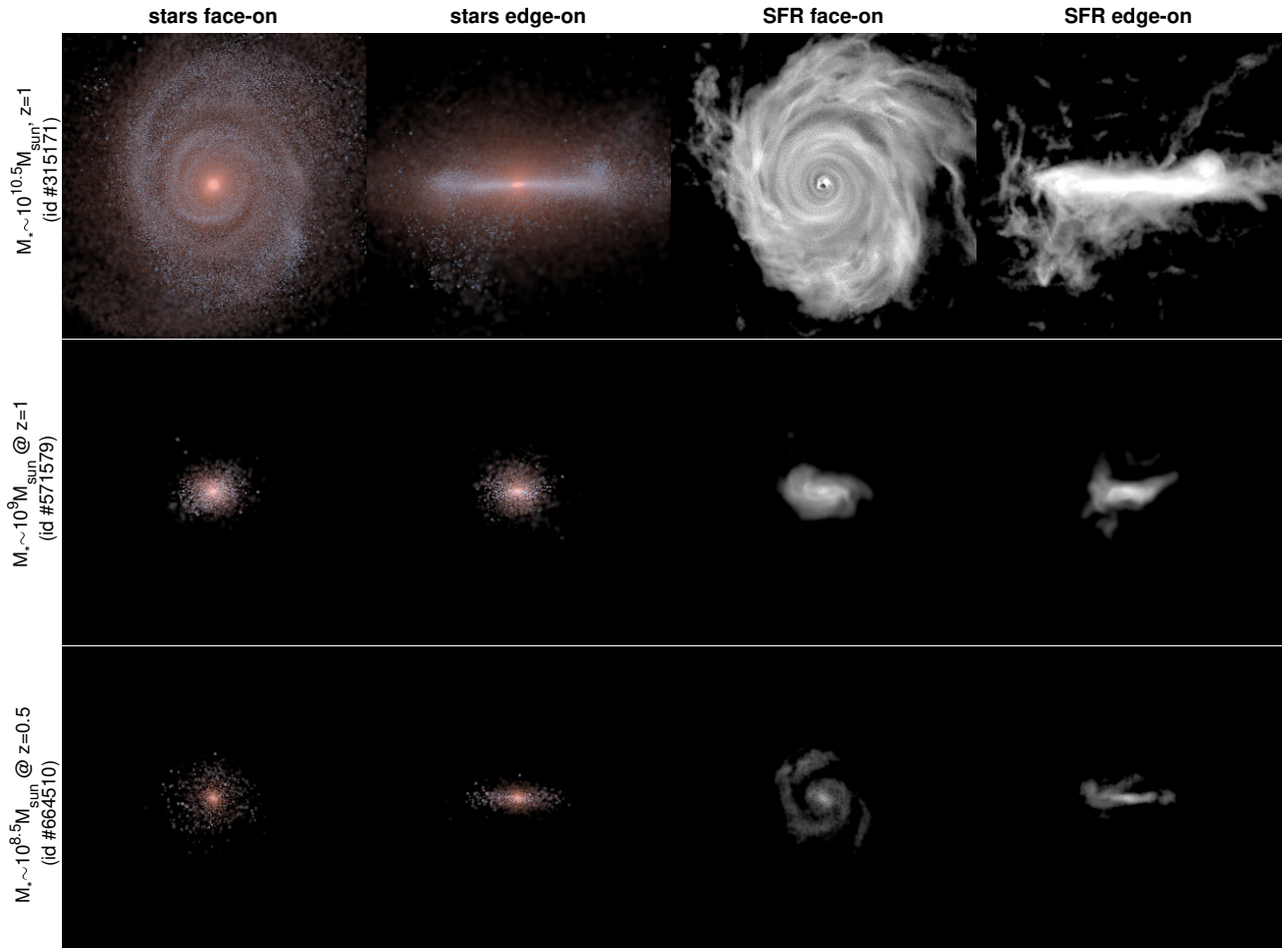
We select 100 SFGs from TNG50 at each of the  $z = 0.5$  and  $z = 1.0$  snapshots with stellar masses in the range  $10^{8.5} M_\odot < M_\star < 10^{10.5} M_\odot$ . We selected SFGs with specific SFR within  $\pm 2\sigma$  from the median sSFR, excluding galaxies with  $\text{sSFR} < 10^{-11} \text{ yr}^{-1}$  in order to mimic the observational selection on SFGs with [O II] emission. From this sample, we randomly select the final sample to have a uniform distribution in  $\log M_\star$  and limited the sample to the range of sizes matching the UDF sample, namely from 1.5 to 6.5 kpc (see Sect. 4). This resulted in a sample of 158 SFGs.

Figure 3 shows the location of the sample of 158 SFGs in the size–mass and sSFR–mass scaling relations. In both panels, the gray points and contours represent the distributions for the  $z = 1$  TNG50 SFGs and the red symbols represent the 158 selected SFGs at  $z = 0.5$  and  $z = 1.0$ . On the left panel, the gray band represents the size–mass relation from van der Wel et al. (2014) and on the right panel, the gray band represents the main-sequence for UDF SFGs (Boogaard et al. 2018). In the left (right) panel, the  $z = 0.5$  galaxies are rescaled to  $z = 1$  according to the size (SFR) evolution found by van der Wel et al. (2014) (Whitaker et al. 2014), respectively. This figure shows that we selected SFGs with properties representative to the full underlying population around the size and SFR scaling relations for SFGs.

Finally, Fig. 4 shows high-resolution images of three representative star-forming galaxies where the two left columns show the stellar light (dust-free color composite of the (SDSS)r-g-(Johnson)B bands) and the two right columns show the SFR in the gas phase, face-on and edge-on.



**Fig. 3.** Sizes and SFRs of the 158 galaxies selected from the overall TNG50 galaxy population. *Left:* size-mass relation for the selected TNG50 for the mocks where the sizes are half-SFR sizes (calculated in face-on projection and without any dust attenuation). The open (solid) squares represent the  $z = 0.5$  ( $z = 1$ ) galaxies where the sizes for the  $z = 0.5$  galaxies are adjusted to  $z = 1$  according to the  $(1+z)^{-0.5}$  evolution found by van der Wel et al. (2014). The background gray points and contours represent the size-mass distribution for the  $z = 1$  TNG50 galaxy population. The solid line (gray band) represents the size-mass relation for late types from Mowla et al. (2019) (van der Wel et al. 2014), respectively. *Right:* SFR-mass or “main-sequence” relation for the selected TNG50 galaxies (red dots, where SFRs for the  $z = 0.5$  galaxies are adjusted to  $z = 1$  according to the  $(1+z)^{2.2}$  evolution found by Whitaker et al. 2014). The background gray points and contours represent the SFR-mass distribution for the  $z = 1$  TNG50 galaxy population. For comparison, we show with the gray band the  $z = 1$  main-sequence from the MUSE UDF analysis of Boogaard et al. (2018).



**Fig. 4.** Visual representations of three example TNG50 star-forming galaxies from the set analyzed in this work. The *two columns on the left* represent stellar light (dust-free color composite of the (SDSS)r-g-(Johnson)B bands) and the *two on the right* the SFR in the gas phase. Each panel is 30 kpc on a side.

### 3.2. Simulated MUSE cubes

Each of the 158 simulated SFGs is processed in the following manner to generate several mock MUSE mini-cubes, for a total number of mock cubes of 790. First, a cube of two spatial dimensions with bounds  $[-N_r/2\Delta_r, N_r/2\Delta_r]$  and one velocity dimension with bounds  $[-N_v/2\Delta_v, N_v/2\Delta_v]$  is generated with  $N_r = 30$  pixels in each spatial dimension and  $N_v = 40$  pixels in the velocity dimension. For  $z = 1$  ( $z = 0.5$ ), we use voxels of size  $\Delta_r = 1.65$  kpc (1.25 kpc) and  $\Delta_v = 50$  km s<sup>-1</sup> (65 km s<sup>-1</sup>), respectively, which corresponds to the MUSE instrument specifications of 0.2 arcsec and 1.25 Å at a rest-frame wavelength of  $\lambda_{\text{rest}} = 3728$  Å (Bacon et al. 2017). Second, the center of this cube is placed at the position of the most bound resolution element of the simulated galaxy, which generally is very close to the center of rotation, and at the velocity of the galaxy center-of-mass. Third, the cube is rotated such that the plane defined by the two spatial dimensions is perpendicular to the eigenvector of the moment of inertia tensor of the galaxy that has the smallest eigenvalue, such that the galaxy appears “face-on”.

For each galaxy, we apply further rotations to generate mock cubes for 5 inclinations ( $i = 15, 30, 45, 60$  and  $75^\circ$ ), each at a random azimuthal orientation  $\phi$ <sup>7</sup>. The SFR in each voxel of the cube is then calculated by summing up the contributions from all simulation gas cells using a Gaussian kernel representing the Point-Spread-Function (PSF) and Line-Spread-Function (LSF) appropriate for non-AO MUSE observations. In particular, for  $z = 1$  ( $z = 0.5$ ) the PSF has a Moffat profile with  $\beta = 2.5$  and a  $FWHM_r$  of 0.625 arcsec (0.675 arcsec) (Bacon et al. 2017), and the LSF has a Gaussian profile with  $FWHM_v = 2.55$  Å (2.75 Å), respectively. The PSF and LSF FWHMs correspond to 5.15 kpc (4.25 kpc) and to 100 km s<sup>-1</sup> (143 km s<sup>-1</sup>), for  $z = 1$  ( $z = 0.5$ ), respectively.

Finally, we add noise to the mock MUSE cubes in order to match the range of S/N (spaxel<sup>-1</sup>) of our MUSE observations, which have  $S/N_{\text{max}}$  of a few to  $\sim 40$  (see Sect. 4). For galaxies with  $\log M_\star/M_\odot > 9$ , we set the noise to 0.001 (0.0002) SFR yr<sup>-1</sup>, respectively.

### 3.3. Reference measurements

In TNG50, we measure the following quantities: the sAM, the maximum rotation velocity  $V_{\text{max}}$  and velocity dispersion  $\sigma_t$ , as follows.

**Specific angular-momentum.** The SFR-weighted  $\tilde{j}_\star(r)$  is calculated using Eq. (1) with  $\rho(\mathbf{x})$  as the star-forming gas density, which corresponds to a [O II] weighting, using the 3D positions, velocities and densities of all SF gas at a given radius. We then use the cumulative profile  $\tilde{j}_\star(<r)$  to then define the total sAM from  $\max(\tilde{j}_\star(<r))$ .

**Velocity dispersion.** The gas velocity dispersion  $\sigma_t$  is defined as the 1D line-of-sight dispersion assuming isotropy, namely it is equal to  $\sigma_{3D}/\sqrt{3}$ . Here,  $\sigma_{3D}$  is the average (SFR-weighted) of the internal velocity dispersion of star-forming gas inside kpc-sized patches at galacto-centric radii of 1.5–2.5  $R_e$ , a method similar to Pillepich et al. (2019). In order to account for thermal broadening for  $T = 10^4$  K gas, we incorporate a  $\sigma_{\text{th}} \approx 15.7$  km s<sup>-1</sup> component into  $\sigma_{3D}$  by adding it in quadra-

ture<sup>8</sup>. This definition of line-of-sight SFR-weighted velocity dispersion at  $\sim 2R_e$  has the advantage that it closely mimics our observations  $\sigma_t(2R_e)$  (see Sect. 2.3).

**Rotational velocity.** The rotation velocity  $V$  is calculated as the SFR-weighted mean of the azimuthal velocities of the same patches used for the calculation of the velocity dispersion.

### 3.4. Robustness of $\tilde{j}_\star(3D)$ from TNG50

We now apply the methodology described in Sect. 2.3 to the sample of 790 mock cubes of 158 simulated galaxies in order to test the performances of GAIPAK<sup>3D</sup> in recovering the morphological (sizes, inclination) and kinematic parameters of realistic galaxies. We find that the inclination is recovered with a relative error of  $\pm 12^\circ$  provided that  $i \geq 30^\circ$ , as found in Contini et al. (2016) (see also Bouché et al. 2015). Consequently, we restrict the analysis to mock cubes with  $i \geq 30^\circ$ .

Figure 5 shows the sAM profile  $\tilde{j}_\star(<r)$  found when applying Eq. (2) and the 3D methodology described in Sect. 2.3 on the massive galaxy shown at the top of Fig. 4. The 5 panels show the  $\Sigma_{\text{sfr}}$  map, the SB profile, the intrinsic velocity field, the intrinsic velocity profile, and the intrinsic  $\tilde{j}_\star$  profile, respectively. The velocity and SB profile are computed on the pseudo-slit, represented by the two horizontal gray lines. The light gray solid lines represent the profiles recovered from our algorithm for each inclination ( $i \geq 30^\circ$ ), each performed on 5 orientations in this case. The red solid lines in columns 2, 3 and 4 represent the  $\Sigma_{\text{sfr}}$ ,  $v(r)$  and  $\tilde{j}_\star$  profiles determined directly from the TNG50 data. In the right most panel, the blue horizontal tick marks show our estimates  $\tilde{j}_\star(3D)$ , while the red horizontal tick marks show  $\tilde{j}_\star$  from RF12 (Eq. (3)). Depending on the steepness of the  $v(r)$  profile, the RF12 approximation can lead to an over-estimation of the total angular momentum by 15–25% for the reasons described in Sect. 2. Figure 5 suggests that our 3D method is able to recover the intrinsic  $\tilde{j}_\star(<r)$  profile with less bias, even when the rotation curve deviates from our assumed parametrization  $v(r) = \tanh$ . Next, we investigate the difference between the estimated and true  $\tilde{j}_\star$  as a function of S/N.

Figure 6(left) shows the measured total angular momentum,  $\tilde{j}_\star(3D)$ , as a function of the true angular momentum (SFR-weighted) as measured directly from the simulation output (bottom subpanel), and their relative difference,  $dj/j \equiv (\tilde{j}_\star(3D) - j_{\text{true}})/j_{\text{true}}$  (top subpanel). The points are colored according to  $M_\star$ . The red circles represent the median of  $dj/j$  whose error-bars represent the  $1\sigma$  standard deviation.

The histogram in the top panel of Fig. 6(left) shows the distribution of the relative errors  $dj/j$ . This histogram shows that globally our method does recover the intrinsic angular momentum with no apparent bias. We can quantify this bias further as a function of galaxy mass in Fig. 6(right). Figure 6(right) shows, for 1-dex bins in  $\log M_\star$  (at 8.5, 9.5 and 10.5), from top to bottom, the distributions of  $dj/j$  resulting from our 3D method (left column) or the RF12 method (right column). The red solid line represents the continuous density estimation of the distributions using a Gaussian kernel with bandwidth of 0.2. Quantitatively, the mean relative error  $dj/j$  for our 3D methodology is  $< 5\%$ , while for the intermediate and lower mass bins, the RF12

<sup>8</sup> This approach follows in spirit the calculations in Appendix A of Pillepich et al. (2019). However, it is important to note that Pillepich et al. (2019), in method (ii) of their appendix, have inadvertently added  $\sigma_{\text{th}} \approx 15.7$  km s<sup>-1</sup> to their line-of-sight velocity dispersions, while for a  $T = 10^4$  K ideal monoatomic Hydrogen gas that value corresponds to the 3D velocity dispersion, as implemented in this work.

<sup>7</sup> In addition, 9 galaxies were tested with 5 different azimuthal orientations for each inclination.



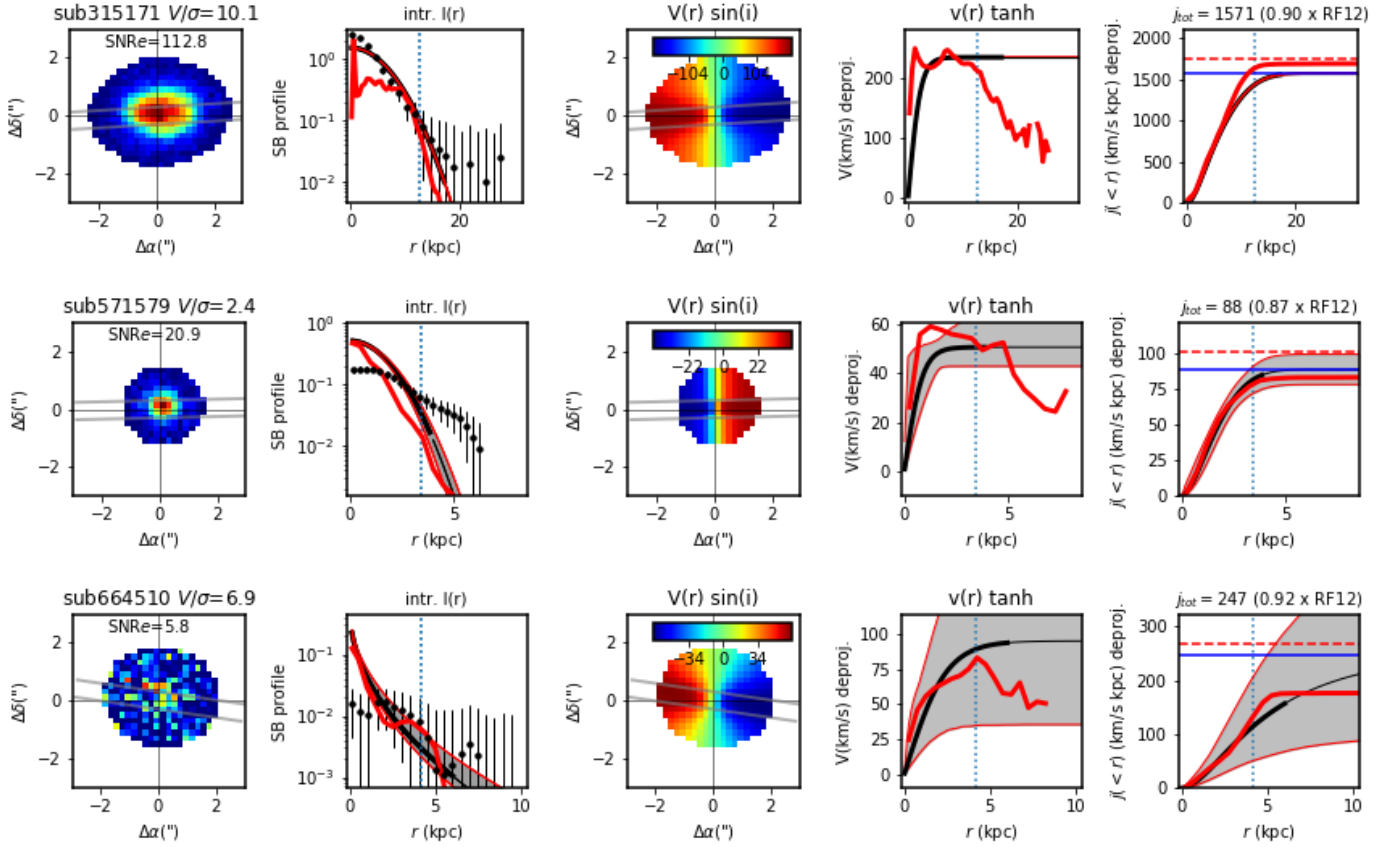


**Fig. 5.** Example of GAIPAK<sup>3D</sup> fits for three SFGs from TNG50 shown in Fig. 4. The columns show the flux map, the flux profile  $\Sigma(r)$ , the intrinsic velocity field, the deprojected velocity profile and the deprojected angular momentum profile, *from left to right* respectively. The 1D profiles are computed along the pseudo-slit shown in the *first and third columns* by the gray lines. In the *second column*, the SB profile for a single orientation is shown (black points). In the *second, fourth and fifth columns*, the solid gray curves show the model fits for the various inclinations and orientations. The red solid lines represent the true profiles determined directly from the TNG50 data. The vertical dotted lines represent twice the half-light radius ( $R_{1/2,\text{SFR}}$ ). The horizontal blue lines show the total modeled angular momentum  $j_{3D}$ , while the horizontal red lines show the total  $j$  from RF12 (Eq. (3)), which can lead to over-estimation of the total angular momentum by 10–20%.

approximation (Eq. (3)) can lead to a significant bias of  $\approx 10$ –15% for the reasons discussed in Sect. 2. For the most massive galaxies with  $M_\star > 10^{10} M_\odot$ , and with  $\log \tilde{j}_\star > 3$ , our method underestimates  $\tilde{j}_\star$  compared to RF12, but it is important to note that our sample in the UDF (Sect. 4) has only a handful of SFGs in this regime.

The width of the distributions shown in Fig. 6 is consistent with the errors obtained with our methodology. Indeed, the width of the ratios of the errors to  $dj$  is consistent with a (Cauchy) distribution<sup>9</sup> of width unity. This implies that the errors obtained from our methodology are broadly representative of the true error  $dj$  on the measurement.

We return now to the top panel of Fig. 6 where the relative difference  $dj/j$  is plotted as a function of the effective  $S/N$ ,  $S/N_{\text{eff}}$ , following the discussion in Bouché et al. (2015). This effective  $S/N$  accounts for the fact that surface brightness (SB) alone is not sufficient to determine the accuracy in the fitted parameters, given that the compactness of the galaxy with respect to the PSF plays also an important role. As discussed in Refregier et al. (2012), in the presence of a PSF convolution, the relative errors on the major-axis  $a$  scales as

$$\frac{\sigma(a)}{a} \propto A_0^{-1} (1 + R_{\text{PSF}}^2/R_e^2), \quad (5)$$

<sup>9</sup> The few outliers are producing a distribution with a heavier tail than a Normal distribution.

where  $A_0$  is the observed central surface brightness in the central voxel,  $R_{\text{PSF}}$  is the radius of the PSF ( $R_{\text{PSF}} \equiv FWHM/2$ ) and  $R_e$  the intrinsic half-light radius. After performing a Taylor expansion around  $R_{\text{PSF}}/R_e \sim (1 - x)$  with  $x \equiv (R_e - R_{\text{PSF}})/R_e$  and  $|x| \ll 1$ , one finds that Eq. (5) becomes in the regime where  $R_{\text{PSF}}/R_e$  is  $\approx 1.0$  (see Bouché et al. 2015):

$$\begin{aligned} \frac{\sigma(a)}{a} &\propto \left( \frac{R_e}{R_{\text{PSF}}} A_0 \right)^{-1} \\ &\propto \left( \frac{R_e}{R_{\text{PSF}}} S/N_{\text{max}} \right)^{-1}. \end{aligned} \quad (6)$$

The last step follows from the simple argument that a given exposure time sets the surface brightness limit per voxel, and hence the maximum  $S/N$  (in the central voxel or spaxel),  $S/N_{\text{max}}$ , is directly proportional to  $A_0$ .

Considering the sAM is essentially determined by the product of  $R_e$  and  $V_{\text{max}}$ , one can thus expect that the accuracy of  $j$  follows Eq. (6), which is represented by the gray curve in the top panel of Fig. 6.

Finally, we end this section by quantifying the potential difference between the SFR-weighted  $\tilde{j}_\star$  and the stellar mass-weighted  $j_\star$  because in observations of high-redshift galaxies, as in Sect. 4, one is often limited to the SFR-weighted  $\tilde{j}_\star$ . Using TNG50  $z = 1$  SFGs in the parent sample, Fig. 7 shows the relation between  $\tilde{j}_\star$  and  $j_\star$ . While this figure shows that

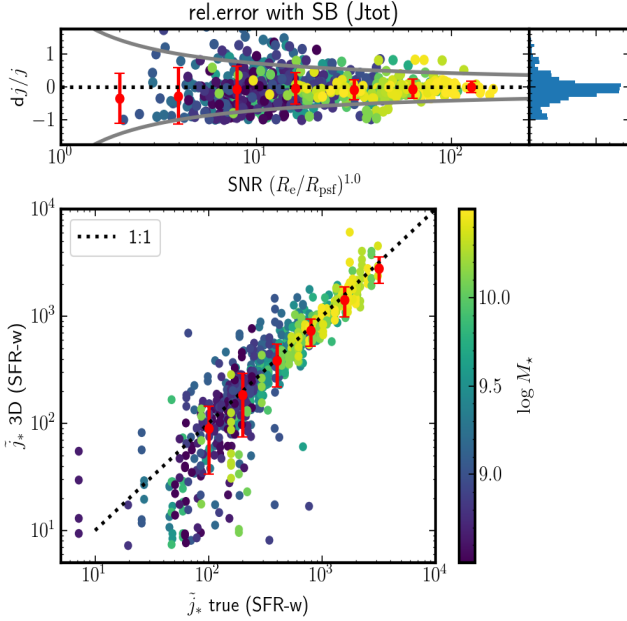


**Fig. 6.** Reliability of our sAM estimator. *Left: bottom panel:* total SFR-weighted sAM,  $\tilde{j}_*$  (in  $\text{km s}^{-1} \text{kpc}$ ), as a function of the true angular momentum (SFR-weighted) for the 790 mock galaxies. *Top panel:* relative error  $(\tilde{j}_* - j_{\text{true}})/j_{\text{true}}$  as a function of the effective S/N (see text) along with the histogram of  $d\tilde{j}_*/\tilde{j}_*$ . The points are colored according to the stellar mass in both panels. The red circles represent the median  $d\tilde{j}_*/\tilde{j}_*$  whose errorbar represent  $1\sigma$ . *Right:* relative error  $(d_j/j \equiv \tilde{j}_* - j_{\text{true}})/j_{\text{true}}$  for each mass bin of 1 dex centered on  $\log M_* = 8.5, 9.5, 10.5$ , from top to bottom. The histograms are weighted by the errors. *Left (right) panels:* distributions of  $d\tilde{j}_*/\tilde{j}_*$ , in three mass bins, resulting from the 3D method (the Eq. (3) approximation), respectively. The red solid line represents the continuous density estimation of the distributions using a Gaussian kernel with bandwidth of  $\sim 0.2$ . This shows that, for massive galaxies ( $M_* > 10^{10} M_\odot$ ), the Eq. (3) approximation is less biased, while for galaxies with  $M_* < 10^{10} M_\odot$ , the 3D method is less biased.

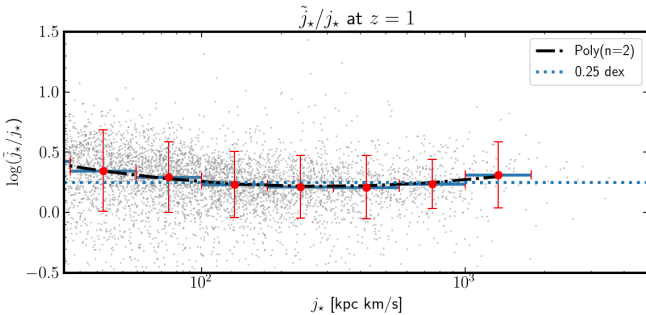


**Fig. 7.** Relation between the stellar sAM  $j_*$  and  $\tilde{j}_*$  for  $z = 1$  TNG50 SFGs. The solid points with errorbars represent the median difference between the two as a function of the stellar angular momentum, where the error bars represent the standard deviation. Thus, the SFR-weighted sAM,  $\tilde{j}_*$ , is higher by  $\approx 0.25$  dex (dotted line) compared to  $j_*$  over a wide range of sAM from 50 to 2000  $\text{km s}^{-1} \text{kpc}$ . A second order polynomial fit is shown with the dot-dashed black line.

the relation becomes non linear in the low mass regime, with  $\log j_* < 1.5$ , (as found by El-Badry et al. 2018, in the FIRE simulations), it also shows that, on average,  $\log \tilde{j}_*$  is an estimate of  $\log j_* + 0.25$  dex over a wide range of sAM from 50 to 2000  $\text{km s}^{-1} \text{kpc}$ , which is the relevant range for our study.

## 4. Application to UDF galaxies

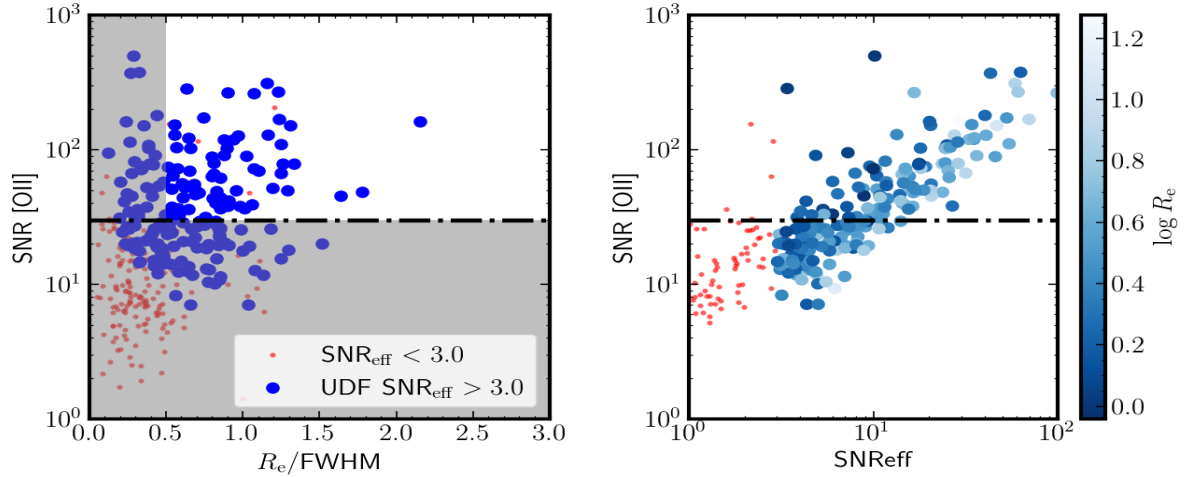
### 4.1. Sample

We exploit the  $3' \times 3'$  observations taken with the MUSE instrument over the *Hubble* Ultra Deep Field (HUDF; Bacon et al. 2017) to investigate the angular momentum of intermediate redshift galaxies using the methodology presented in Sect. 2.3. The

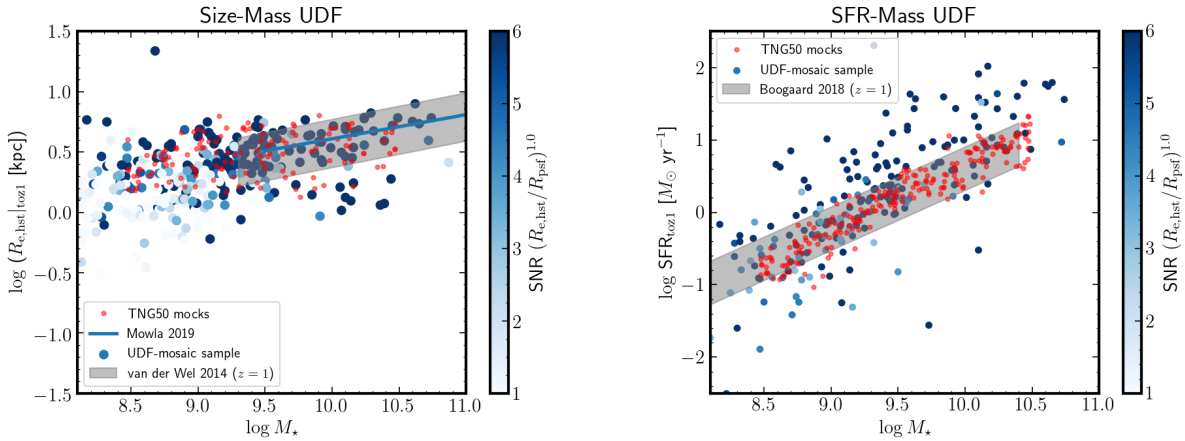
observations were performed on a mosaic of nine  $1' \times 1'$  10 h pointings and contain a single  $1' \times 1'$  27 h pointing, but we concentrate on the mosaic sample to ensure a homogenous selection. In the MUSE UDF mosaic, there are 494 [O II] emitters (Inami et al. 2017). These [O II] emitters have stellar masses ranging from  $10^{7.5}$  to  $10^{11} M_\odot$ , where the stellar masses are estimated (as in Boogaard et al. 2018) using the stellar population synthesis (SPS) code FAST (Kriek et al. 2009) assuming a Chabrier (2003) initial mass function with an exponentially declining star formation history. As discussed in the next section, most [O II] emitters are rather faint, with only about  $\sim 50\%$  of these having a S/N above  $\sim 3$ .

Figure 8 (left) shows the S/N of the total [O II] flux as a function of the “resolved size” ( $R_e$  divided by the PSF FWHM) for the sample of SFGs, where the blue (red) points are SFGs with a  $S/N_{\text{eff}} > 3.0$  ( $< 3.0$ ), respectively. For comparison, the selection used in Abril-Melgarejo et al. (2021) is shown with the gray bands. The right panel compares the effective S/N and the total S/N, where the points are color-coded as a function of size  $R_e$ , displaying the common surface-brightness biases. This figure shows that a  $S/N_{\text{eff}} \approx 3$ , as determined in the previous section, opens the possibility to study the kinematics of faint galaxies, enlarging the sample by 30–50%.

Figure 9 shows the properties of the UDF sample in terms of sizes and SFRs as in Fig. 3. The sizes are the continuum-based  $R_e$  obtained from HST/F160W from van der Wel et al. (2014) and the SFRs are derived from SED fitting. The left panel shows the sample in the size-mass plane color coded as a function of the effective S/N, where the sizes were adjusted to  $z = 1$ . For comparison, we show the size-mass scaling relation of van der Wel et al. (2014) and Mowla et al. (2019) down to  $M_* \sim 10^8 M_\odot$ . The TNG50 mocks used in Sect. 3 are represented with the red small circles. The right panel shows the



**Fig. 8.** *Left:* following [Abril-Melgarejo et al. \(2021\)](#), we show the S/N of the total [O II] flux as a function of the resolved ratio ( $R_{e,hst}/PSF$  FWHM) for the sample of SFGs. The gray bands represent the selection of resolved galaxies in [Abril-Melgarejo et al. \(2021\)](#), consisting of  $S/N > 30$  and  $R_{e,hst}/FWHM > 0.5$ . *Right:* comparison between the total [O II] S/N and the effective S/N (Eq. (6)), color-coded with  $R_e$ . In both panels, the red points are galaxies with  $S/N_{eff} < 3.0$ , while the blue points correspond to galaxies with  $S/N_{eff} > 3.0$ .



**Fig. 9.** Comparison of selection techniques. *Left:* size-mass relation for the SFGs in the UDF mosaic sample (blue circles). The sizes are adjusted to  $z = 1$  according to the  $(1+z)^{-0.5}$  evolution found by [van der Wel et al. \(2014\)](#). The solid line (gray band) represent the size-mass relation of [Mowla et al. \(2019\)](#) ([van der Wel et al. 2014](#)). *Right:* main-sequence relation for the SFGs in the UDF mosaic sample. The SFRs are adjusted to  $z = 1$  according to the  $(1+z)^{1.74}$  evolution of [Boogaard et al. \(2018\)](#) whose  $z = 1$  main sequence is represented by the gray band. In both panels, the points are color-coded according to effective S/N. For comparison we show the properties of the mock 158 galaxies (Sect. 3.2) as red circles.

main-sequence or the SFR-mass plane where the points are color-code as a function of size. The points are scaled to  $z = 1$  where we used the main-sequence redshift evolution of [Boogaard et al. \(2018\)](#).

#### 4.2. Size estimates

The first part of the methodology outlined in Sect. 2.3 is to determine the morphological parameters (size, inclination) by performing two dimensional Sérsic fits to the [O II] flux maps. Given that the UDF data set has extensive *Hubble Space Telescope* (HST) coverage, we first ask whether our Sérsic fits on [O II] (from ground-based MUSE observations at a resolution of  $0.62''$ ) are able to recover the HST morphological parameters (at a resolution of  $0.15''$ ) from their stellar continuum.

Given that the galaxy half-light radius plays a crucial role in determining  $j$ , we show in Fig. 10(left) the intrinsic [O II]-based  $R_e$  found from our MUSE data compared to the continuum-based  $R_e$  obtained from HST/F160W from [van der Wel et al. \(2014\)](#). This figure shows that there is a good agreement between the

two quantities, provided that the size-corrected “effective S/N” (Eq. (6)) in the brightest voxel, namely  $S/N_{max} \times (R_e/R_{psf})$  where  $S/N_{max}$  is the S/N in the central voxel and  $R_{psf}$  is the PSF radius (half-FWHM), is  $\gtrsim 3$ . The S/N level of  $\sim 3$  is our fiducial threshold for the remainder of our analysis. From the 494 SFGs in the 9 arcmin<sup>2</sup> UDF mosaic, there are 182 galaxies meeting this criterion.

This demonstrates that our algorithm is able to determine  $R_e$  with sufficient accuracy down to  $\approx 1$  kpc. This is beyond the 3 kpc limit of other IFS surveys as the parameter space between  $1 < R_e < 3$  kpc (and  $10^8 < M_* < 10^{9.5} M_\odot$ ) has been relatively unexplored so far with any of the large IFS surveys (e.g., [Burkert et al. 2016](#); [Swinbank et al. 2017](#); [Harrison et al. 2017](#)). Figure 10 shows the location of half-light radii  $R_e$  of our subsample of 182 galaxies as a function of redshift where the parameter space probed by [Swinbank et al. \(2017\)](#) is shown as the gray band. This figure shows that, compared to [Swinbank et al. \(2017\)](#), our sample includes galaxies with sizes in the range 1–3 kpc, previously inaccessible from ground-based observations.

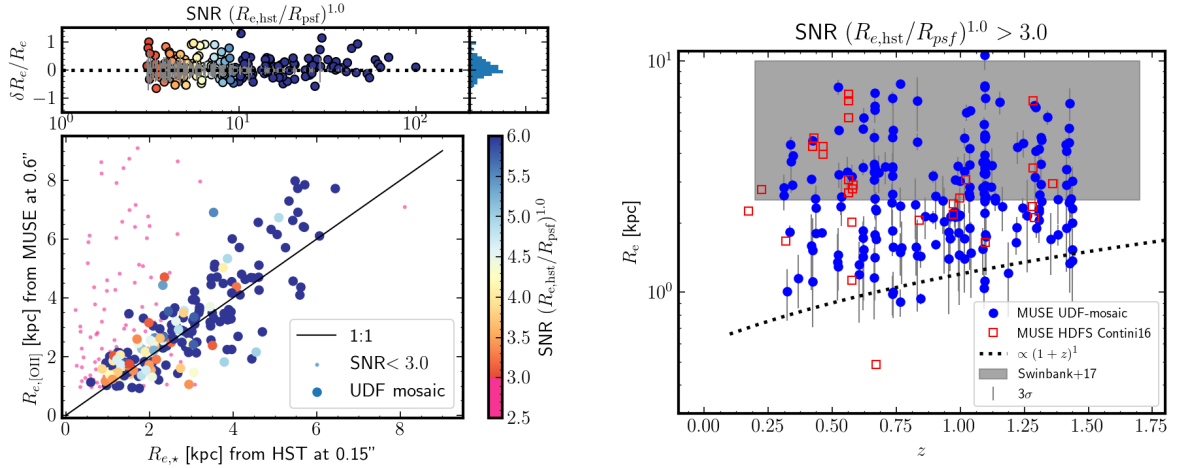


**Fig. 10.** *Left:* comparison between [O II]-based sizes  $R_e$  from MUSE (at  $FWHM \approx 0.7''$  resolution) versus  $H$ -band continuum  $R_{e,*}$  from HST/F160W at  $\approx 0.15''$  resolution, for the full sample of 494 SFGs, where the points are color-coded according to Eq. (6). The *top panel* shows the relative error  $\delta R_e/R_e$  as a function of the effective S/N (see text) and the side histogram shows its distribution. The gray errorbars represent the  $3\sigma$ , statistical uncertainties. This shows that our MUSE-[O II] sizes are of sufficient accuracy down to  $\approx 1$  kpc, provided that the effective S/N is  $\gtrsim 3$ . *Right:* sizes  $R_e$  (from HST/F160W) as a function of redshift for 182 galaxies in the MUSE UDF-mosaic field whose effective S/N is sufficient. The gray region represents the region probed by Swinbank et al. (2017). The dashed line represents  $\propto (1+z)^1$ . The vertical error bars are  $3\sigma$ .

#### 4.3. The angular momentum of SFGs at $0.4 < z < 1.4$

We apply the two-step methodology outlined in Sect. 2.3 on the MUSE UDF sample of 494 [O II] emitters. We find that 182 meet our S/N threshold discussed above, namely with effective  $S/N \gtrsim 3$ . The sample is thus made of all [O II] emitters in the UDF MUSE mosaic with sufficient S/N and is composed of SFGs with Sérsic profiles that are mostly exponential. Two thirds of the sample has  $n = 1.0$ , while the remainder has  $n = 0.5$ . The distribution of inclinations  $i$  is consistent with an unbiased sample, namely  $P(\cos(i)) \sim b/a$  is flat for  $i > 30$  ( $b/a < 0.86$ ). As discussed in Sect. 2.3, we compute the angular momentum of the star-forming gas  $\tilde{j}_*$  by integrating Eq. (2) from the flux  $\Sigma(r)$  and kinematic  $v(r)$  GALPAK<sup>3D</sup> fits.

Figure 11(left) shows the resulting  $\tilde{j}_* - M_*$  sequence for the 182 galaxies in our sample. This figure shows the sAM  $\tilde{j}_*$  (SFR weighted) as a function of stellar mass  $M_*$  where the points are color-coded according to  $\log(V_{\max}/\sigma_t)$  where  $\sigma_t$  is the outer velocity dispersion (see Sect. 2.3) measured with GALPAK<sup>3D</sup> (defined as in Cresci et al. 2009). The right axis shows the corresponding stellar mass-weighted  $j_*$  from the typical offset found in Fig. 7.

In Fig. 11(left), the dotted-dashed blue (red) line show the  $j_* - M_*$  sequence for late (early) type galaxies at  $z = 0$  from Fall & Romanowsky (2018), respectively. The dotted line shows the  $z = 0$  sequence for the sample of disk galaxies of Posti et al. (2018a) which has a pure power-law sAM  $j_* \propto M_*^{0.55}$  (see also Mancera Piña et al. 2021). The thin black dotted curve represents the selection limit of our observations of  $V_{\max}^2 + \sigma_t^2 = K^2$  described in Appendix B.

In a cosmological framework, the  $j_*$  of a galaxy with stellar mass  $M_*$  that resides in a virialized halo of mass  $M_{\text{vir}}$  at a given redshift  $z$  can be written as (following Mo et al. 1998; Navarro & Steinmetz 2000; Romanowsky & Fall 2012; Obreschkow et al. 2015; Burkert et al. 2010, 2016; Stevens et al. 2016; Swinbank et al. 2017):

$$\begin{aligned} j_* &\propto \lambda f_j f_m^{-2/3} H(z)^{-1/3} \Delta_c(z)^{-1/6} M_*^{2/3} \\ &\propto \lambda f_j f_m^{-2/3} M_*^{2/3} (1+z)^{-1/2}, \end{aligned} \quad (7)$$

where  $\lambda$  is the halo spin parameter,  $f_m \equiv M_*/M_h$  is the stellar-to-halo mass ratio,  $f_j \equiv j_*/j_h$  is the  $j$  retention factor (or the stellar-to-halo sAM ratio), and the expected  $(1+z)^{-1/2}$  redshift evolution follows from  $H(z)$ , the Hubble parameter and  $\Delta_c(z)$ , the halo over-density relative to the mean density of the universe (Bryan & Norman 1998). For constant  $f_m$  in massive galaxies, the  $j_* - M_*$  relation is expected to be  $\propto M_*^{2/3}$ , while in low-mass galaxies,  $j_*$  should be  $\propto M_*^{1/3}$  given that abundance matching shows that (Moster et al. 2010; Dutton et al. 2010; Behroozi et al. 2013)  $f_m \propto M_*^{1/2}$ . In other words, the  $j_* - M_*$  relation should have a slope of 2/3 (1/3) in the high-(low) mass regime, respectively, provided that the retention fraction  $f_j$  is constant (see Posti et al. 2019, for detailed discussions).

Following Romanowsky & Fall (2012), Eq. (7) becomes

$$\begin{aligned} j_*(M_*, z) &= 1010 \text{ km s}^{-1} \text{ kpc} \frac{\lambda}{0.034} f_j f_m^{-2/3} M_{*,10}^{2/3} (1+z)^{-1/2} \\ &= 715 \text{ km s}^{-1} \text{ kpc} \frac{\lambda}{0.034} f_j f_m^{-2/3} M_{*,10}^{2/3} (1+z)_1^{-1/2}, \end{aligned} \quad (8)$$

where  $M_{*,10} \equiv M_*/10^{10} M_\odot$ ,  $\lambda$  the halo spin parameter and  $(1+z)_1 = (1+z)/2$ . Eq. (8) is shown as the solid black line in Fig. 11(left), assuming  $f_m$  from abundance matching (Dutton et al. 2010),  $\lambda = 0.034$  from DM simulations (Macciò et al. 2007; Bett et al. 2007, 2010), and  $f_j = 1$ .

##### 4.3.1. The $j - M - (V/\sigma)$ relation

In the local universe, a transition between the late to early type  $j - M$  sequence has also been observed (Romanowsky & Fall 2012; Fall & Romanowsky 2013, 2018; Obreschkow & Glazebrook 2014; Murugesan et al. 2020), where the  $j - M$  relation is a function of the bulge-to-total ratio  $B/T$ . Similarly, Harrison et al. (2017) found, on a sample of 586 SFGs at  $z \approx 0.9$ , that the  $j - M$  relation is a function of Sérsic index  $n$ , where sAM decreases with increasing  $n$ . Cortese et al. (2016), using SAMI, showed that the  $j - M$  relation is a function of the stellar spin parameter,  $\lambda_R$  (as defined in Emsellem et al. 2007), thus defining a continuous sequence in the sAM-stellar mass plane ( $j - M - \lambda_R$ ).

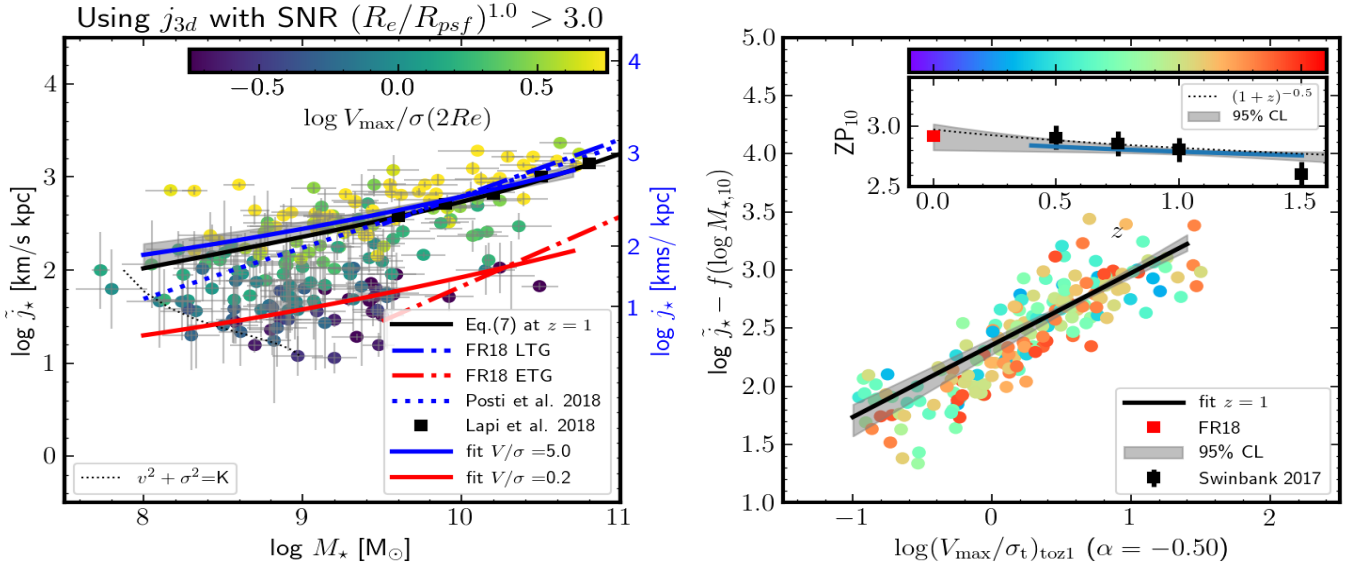


**Fig. 11.** Specific angular momentum for the 182 galaxies in the MUSE UDF mosaic fields with a max  $S/N \gtrsim 3$ . *Left:* total specific angular momentum  $\tilde{j}_\star$  (SFR weighted) as a function of stellar mass  $M_\star$ . The points are color-coded as a function of  $V/\sigma_t$ . The right-axis shows the corresponding  $j_\star$  according to the 0.25dex offset found in Fig. 7. The blue (red) dashed line show the  $j_\star \propto M_\star^{0.6(0.75)}$  sequence for late (early) type galaxies at  $z = 0$  from Fall & Romanowsky (2018, FR18). The dotted line (solid squares) show the  $z = 0$  sAM  $j_\star - M_\star$  sequence from Posti et al. (2018a) (Lapi et al. 2018), respectively. The dotted line show the  $j_\star \propto M_\star^{0.55}$  sequence for  $z = 0$  disk galaxies of Posti et al. (2018a). The solid black line shows the expected  $j_\star - M_\star$  relation from Eq. (8). The solid blue and red lines show the fitted fiducial model from Eq. (9) and the gray band represents the 95% confidence interval. *Right:* normalized AM sequence  $\tilde{j}_\star/f(\log M_\star)$  as a function of  $(V/\sigma_t)_{\text{toz1}}$  (normalized to  $z = 1$  see text), i.e. after taking into account for the redshift evolution of  $\sigma_t(z)$ , where the points are color-coded with redshift. In the inset, we show the redshift evolution of the sAM relation at  $M_\star = 10^{10} M_\odot$  (solid line) at fixed  $(V/\sigma_t)_{\text{toz1}} (=5)$  along with the 95% predictive interval (gray band), with the  $z = 0$  ZP from Fall & Romanowsky (2018) (red square), the Swinbank et al. (2017) binned data (see text), and the expected  $(1+z)^{-0.5}$  evolution (dotted line) from Eq. (8).

At intermediate redshifts, Contini et al. (2016), with only 28  $0.4 < z < 1.4$  galaxies in the MUSE HDFS, found that  $z \approx 1$  SFGs fill a continuous transition between rotation dominated (with  $V/\sigma_t > 1$ ) to dispersion dominated galaxies (with  $V/\sigma_t < 1$ ) where the two populations followed the late/early type sAM sequence of Fall & Romanowsky (2013). This  $V/\sigma$  trend was also present in the high mass sample of Burkert et al. (2016). Here, with our larger sample of intermediate redshift SFGs from the MUSE UDF mosaic 9 arcmin<sup>2</sup> fields, we revisit this question.

To quantify this  $j - M - (V/\sigma)$  relation, we show in Fig. 11(right) the normalized AM sequence  $\tilde{j}_\star/f(M_{\star,10})$  as a function of  $V/\sigma_t$  where the points are color-coded with the redshift  $z$ . The normalization  $f(M)$  removes the mass dependence obtained from the fit (see below). Figure 11 clearly shows that the  $z \sim 1$  AM sequence is actually a 3-dimensional  $j - M - (V/\sigma_t)$  sequence, meaning that the sAM is a strong function of the galaxy dynamical state  $V/\sigma_t$ . This confirms the early results of Contini et al. (2016) and extends the results of Burkert et al. (2016) (their Fig. 2) for high-mass SFGs with  $M_\star > 10^{10} M_\odot$  to low mass galaxies with  $M_\star \sim 10^8 M_\odot$ .

Following Obreschkow & Glazebrook (2014) and Fall & Romanowsky (2018) who fit  $j_\star(M_\star, B/T)$  as a 2-dimensional plane in a 3D space, we fit the AM sequence in Fig. 11 with a 3-dimensional function in  $M_\star$ ,  $V/\sigma_t$  and redshift  $z$ . For this purpose, we use a quadratic polynomial  $f(\log M_\star)$  in  $\log M_\star$ , a linear redshift dependence in  $\log(1+z)$  and a linear relation with  $\log(V/\sigma_t)$  such that:

$$\begin{aligned} \log \tilde{j}_\star &= \alpha (\log M_{\star,10})^2 + \beta \log M_{\star,10} + k + ZP(z) \text{ with} \\ ZP(z) &= a \log(1+z)_1 + b \\ k &= \gamma \log[(V/\sigma_t)_5] \end{aligned} \quad (9)$$

where  $\log M_{\star,10} = \log(M_\star/10^{10} M_\odot)$ ,  $(V/\sigma_t)_5$  is  $V/\sigma_t/5$ , and  $(1+z)_1 = (1+z)/2$ . In this parametrization,  $a$  captures the redshift evolution  $(1+z)^a$  and  $b$  is the zero-point of the sAM relation at  $z = 1$  for rotation dominated SFGs with  $V/\sigma_t = 5$  and  $M_\star = 10^{10} M_\odot$ .

In fitting for the redshift evolution in Eq. (9), a key assumption is often made (e.g., Swinbank et al. 2017), namely that the distribution of  $V/\sigma_t$  is redshift-independent. However,  $V/\sigma_t$  is known to be strongly evolving with redshift (e.g., Förster Schreiber et al. 2006; Genzel et al. 2008; Epinat et al. 2012; Kassin et al. 2012; Wisnioski et al. 2015; Übler et al. 2019). This has two (but related) important consequences. First, any particular definition of disk galaxies (e.g., with a constant cut at  $V/\sigma_t > 1$  or  $> 2$ ) becomes a redshift-dependent selection of the underlying population. Indeed, a population with a  $V/\sigma_t(z)$  distribution evolving with redshift means that a fixed  $V/\sigma_t$  cut (commonly used in the literature) will select a changing fraction of the underlying disk population. Second, this evolution should be taken into account if the redshift evolution  $(1+z)^a$  captured in Eq. (9) is to mean the redshift evolution at a fixed dynamical state or for the median of the population.

Since we aim to compare the sAM sequence  $\tilde{j}_\star - M_\star$  across our wide redshift range 0.4–1.4, the redshift evolution of  $V/\sigma_t$  can bias the  $j - M$  redshift evolution, and cannot be neglected. Thus, the  $k$  term in Eq. (9) ought to be  $k = \gamma \log[(V/\sigma_t)_{\text{toz1}}/5]$ , where  $(V/\sigma_t)_{\text{toz1}}$  is  $(V/\sigma_t)$  corrected to  $z = 1$ . This ensures that we are describing the evolution of the  $\tilde{j}_\star - M_\star - (V/\sigma_t)$  sequence without being impacted from the redshift evolution of  $V/\sigma_t$ .

To estimate  $(V/\sigma_t)_{\text{toz1}}$ , we use the redshift evolution of  $V/\sigma_t$ , discussed extensively in Übler et al. (2019) and Pillepich et al. (2019), which comes primarily from the evolution of  $\sigma_t(z)$  given the negligible evolution of the Tully-Fisher relation

(e.g., Di Teodoro et al. 2016; Übler et al. 2017; Tiley et al. 2019). It can be parametrized as

$$\left(\frac{V}{\sigma_t}\right)(z) \propto (1+z)^q. \quad (10)$$

Ignoring this effect will increase bias the redshift evolution of the  $j-M$  relation, specifically the  $a$  coefficient in Eq. (9) will be biased by approximately  $q \times \gamma$ .

We find that the parameter  $q$  in Eq. (10) can be found by minimizing the  $V/\sigma_t$  distribution over the full redshift range (as discussed in Appendix D). Figure D.1(right) shows that  $q \simeq -0.5$  is most appropriate for the UDF sample where  $\sigma_t \equiv \sigma(2R_e)^{10}$ .

#### 4.3.2. The $j-M-(V/\sigma)$ global fit

We use a Bayesian algorithm to fit the 5 parameters ( $\alpha, \beta, \gamma, a, b$ ) using a Student- $t$  likelihood<sup>11</sup> with the NoU-Turn Sampler (NUTS) from the PYMC3 python package (Salvatier et al. 2016). In Fig. 11, we show the resulting fit to the  $j-M-(V/\sigma_t)$  relation using Eq. (9) whose fitted parameters are listed in Table 1. From this fit, one sees that the  $\tilde{j}_* - M_*$  relation is a nonlinear function of  $M_*$ , as the  $\tilde{j}_* - M_*$  relation flattens toward low masses given that the quadratic factor  $\alpha$  is significantly non zero ( $\alpha = 0.04 \pm 0.01$ ). Specifically, the slope of the sAM relation  $s \equiv d \log \tilde{j}_* / d \log M_*$  goes from  $s \approx 0.5$  at  $\log M_*/M_\odot = 10.5$ , consistent with numerous results at  $z = 0$  (e.g., Obreschcow & Glazebrook 2014; Cortese et al. 2016; Posti et al. 2018a; Fall & Romanowsky 2018) or high-redshifts (e.g., Swinbank et al. 2017; Marasco et al. 2019), to  $s \approx 0.25$  in the low mass regime at  $\log M_* = 8$ . In the remainder of this paper, we use  $f(\log M)$  as short hand for this nonlinear mass dependence in Eq. (9) for the remainder of this work.

This nonlinear  $j-M$  relation is expected from Eq. (7) where the stellar mass fraction  $f_m$  plays a significant role in this mass regime. Together, this result indicates the angular momentum retention fraction  $f_j$  at  $z \sim 1$  is not far from being constant with mass (see Posti et al. 2018b, 2019, for discussions on this at  $z = 0$ ).

#### 4.3.3. The $j-M$ redshift evolution

In regards to the redshift dependence of the sAM sequence, the inset in Fig. 11(right) shows the redshift evolution of the zero-point  $ZP_{10}$  (Eq. (9)) of the  $\tilde{j}_* - M_*$  relation fitted over our redshift range  $0.4 < z < 1.4$  for  $M_* = 10^{10} M_\odot$  and  $V/\sigma_t = 5$ . The red circle shows the RF12  $z = 0$  zero-point, and the squares show the Swinbank et al. (2017) results<sup>12</sup>. The dashed line shows the  $(1+z)^{-1/2}$  expected evolution (Eq. (7)). This panel shows that the sAM relation (at fixed  $V/\sigma_t$ ) is evolving as

$$\tilde{j}_*/f(\log M_*) \propto (1+z)^a,$$

<sup>10</sup> When using the alternative definition of  $\sigma_t \equiv \sigma_0$  (discussed in Sect. 2.3) used in Übler et al. (2019), we find that  $q \simeq -0.7$  to  $-0.8$  very similar to the value of  $-0.8$  we derived from the Übler et al. (2019) data (their Fig. 6).

<sup>11</sup> A Student- $t$  likelihood is preferred over a Gaussian likelihood because it is naturally robust against potential outliers from its larger tail.

<sup>12</sup> For Swinbank et al. (2017), we assumed a mean  $V/\sigma_t = 2.5$  for their  $V/\sigma_t > 1$  sample according to their sample properties. For Romanowsky & Fall (2012), we assumed a  $V/\sigma = 5$  for their disk-dominated sample and shifted their  $j_*$  zero-point to our SFR-weighted  $\tilde{j}_*$  by  $-0.25$  dex.

with  $a = -0.27_{-0.56}^{+0.42}$  (95%) which is consistent with the theoretical evolution  $(1+z)^{-1/2}$  from Eq. (7). This redshift dependence is not consistent with the slope of  $-1$  found by Swinbank et al. (2017) to  $z = 1.5$ , but it should be noted that they did not perform a global fit to their data and that their binned data (squares in the inset of Fig. 11(right) are in fact consistent with a slope of  $-0.5$  up to  $z = 1.0$ , with the  $z = 1.5$  binned data not matching the  $(1+z)^{-0.5}$  trend is most likely due to incompleteness issues at these redshifts.

While Swinbank et al. (2017) and Harrison et al. (2017) found some evidence for a redshift evolution of the  $j-M$  relation with a combined data-set of  $\sim 1000$  SFGs, in contrast, Marasco et al. (2019) found no evidence for a redshift evolution of the  $\tilde{j}_* - M_*$  relation on a subset (made of 17  $z = 1$  disk galaxies with  $M_* > 10^{9.5} M_\odot$ ) of the KROSS and KMOS3D survey. This discrepancy implies no evolution of both the TFR relation and of the size-mass relation, in apparent contradiction to several studies (e.g., Straatman et al. 2017; Übler et al. 2017; van der Wel et al. 2014). This discrepancy could originate from the small sample size, from the different methodologies involved, and/or could be resolved under our  $(V/\sigma_t)$  framework.

## 5. Comparisons to SFGs in TNG50

In order to compare our results on the sAM relation presented in Sect. 4.3 to TNG50, we selected 18000 SFGs at  $z = 0.5, 1.0$  and  $1.5$  from TNG50. We matched the properties of TNG50 SFGs to the UDF SFGs as follows. We first match the SFR distribution by imposing a  $\log(\text{SFR}/[M_\odot \text{ yr}^{-1}]) > -1.5$  as well as impose a similar observational limit of  $\sqrt{V_{\text{max}}^2 + \sigma_t^2} > 30 \text{ km s}^{-1}$ , and then match both the redshift and stellar mass distributions of the UDF sample. The resulting sample is made of 5180 SFGs.

Figure 12(left) shows the SFR-weighted sAM  $\tilde{j}_*$  as a function of  $M_*$  for SFGs in TNG50 with  $M_* > 10^8 M_\odot$ , color-coded with  $(V/\sigma_t)$ . Fig. 12(right) shows the relation between the normalized sAM  $\tilde{j}_*/f(M_*)$  and  $(V/\sigma_t)_{\text{tot}z1}$  that is  $V/\sigma_t$  corrected for its redshift evolution to  $z = 1$  using the scaling  $V/\sigma_t \propto (1+z)^{0.87}$  found in Fig. D.1. In this figure, we show only 1000 SFGs for clarity. Figure 12 shows that SFGs in TNG50 follow similar trends with  $M_*$  and with  $V/\sigma_t$  as in the UDF sample. In particular, the  $\tilde{j}_* - M_*$  relation is also a strong function of  $V/\sigma_t$ .

To quantify potential differences, we applied the same parametric fit as for the UDF sample on a randomly selected subset of 250 galaxies in order to have statistical errors similar to the UDF sample, namely using Eq. (9) with the redshift evolution of  $V/\sigma_t$  (Eq. (10)). The results are listed in Table 1 with and without the correction for the redshift evolution of  $V/\sigma_t$ . One sees that the  $V/\sigma_t$  dependence is stronger in TNG50 than in the UDF sample with  $\gamma \sim 1.3$ , and the redshift evolution for the TNG50 SFGs is consistent with the  $(1+z)^{-0.5}$  expectation, with  $a = -0.45 \pm 0.25$ , against  $a \simeq -0.27_{-0.56}^{+0.42}$  for the UDF SFGs.

We end this section by noting that we found no strong dependence of the sAM with age (formation redshift) or with morphological indicators (Tacchella et al. 2019), such as Gini-M20, and bulge-to-total ratio  $B/T$ .

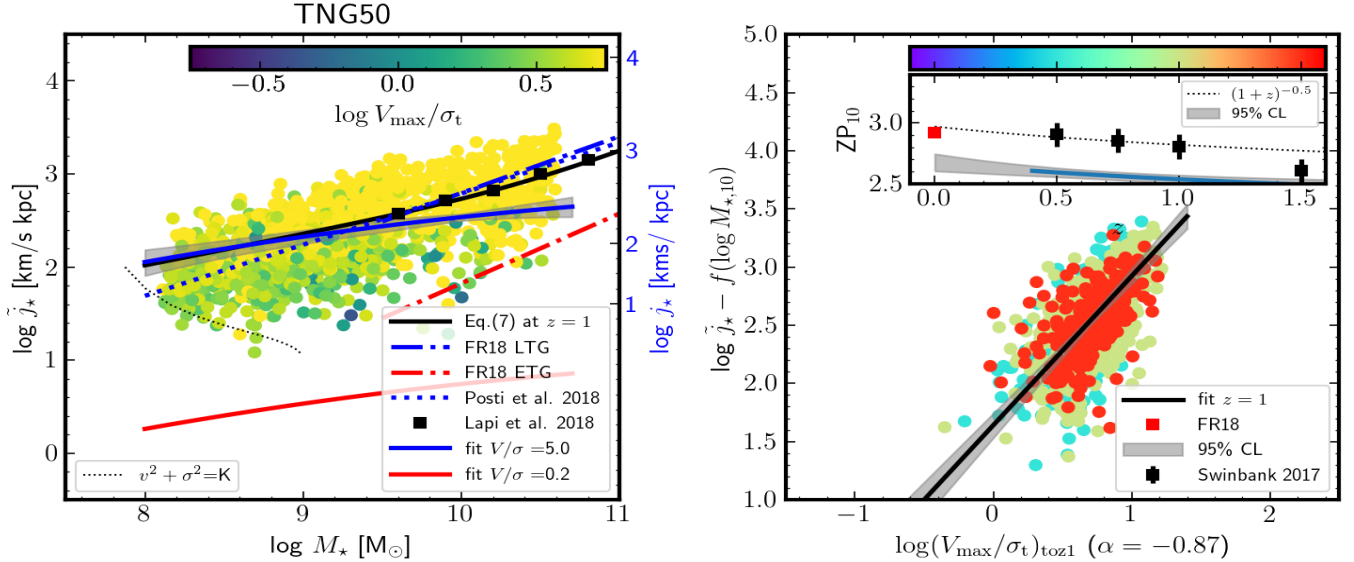
## 6. The $j-M-(V/\sigma)$ relation: implications

As shown in Figs. 11 and 12, the sAM sequence of SFGs in the UDF and in TNG50 represents a strong function of the galaxy dynamical state as characterized by  $V/\sigma_t$ , where rotation dominated SFGs with  $V/\sigma_t \sim 5$  and dispersion dominated SFGs with  $V/\sigma_t = 0.1$  are offset by  $\sim 1$  dex. This result re-inforces

**Table 1.** Fitted parameters to  $\tilde{j}_\star - M_\star$  from Eq. (9).

Data	Model	$\alpha$	$\beta$	$\gamma$	$a$	$b$	$q$
(1)	(2)	(3)	(4)	(5)	(6)	(7)	(8)
UDF	Fiducial	$0.03^{+0.01}_{-0.01}$	$0.37^{+0.09}_{-0.05}$	$0.65^{+0.06}_{-0.08}$	$-0.27^{+0.42}_{-0.56}$	$2.79^{+0.05}_{-0.03}$	-0.5
TNG50	Fiducial	$-0.03^{+0.05}_{-0.05}$	$0.18^{+0.07}_{-0.07}$	$1.28^{+0.10}_{-0.10}$	$-0.45^{+0.24}_{-0.27}$	$2.54^{+0.03}_{-0.04}$	-0.87
TNG50	noVS	$0.05^{+0.09}_{-0.09}$	$0.53^{+0.08}_{-0.12}$	-	$+0.06^{+0.28}_{-0.28}$	$2.78^{+0.03}_{-0.03}$	-

**Notes.** (1) Data set; (2) Model name; (3–7) Parameters from Eq. (9) with 95% confidence levels ( $2\sigma$ ); (8) Redshift evolution of  $V/\sigma_t$  (Eq. (10)).


**Fig. 12.** Same as Fig. 11, but for TNG50 SFGs.

the preliminary results of Contini et al. (2016) on only 27 intermediate redshift SFGs, and extends the similar trend present in Burkert et al. (2016) for massive (with  $M_\star > 10^{10} M_\odot$ ) SFGs.

This  $j - M - (V/\sigma_t)$  relation has important consequences. If SFGs form with high sAM, on the rotation-dominated  $j - M$  sequence, this  $j - M - (V/\sigma_t)$  relation indicates that SFGs may experience a dynamical transformation to lower their sAMs prior to becoming passive, and remain on the early-type  $j - M$  sequence. This might also lead to a morphological transformation as the  $j - M$  residuals also correlate with Sérsic  $n$  (Harrison et al. 2017), but this trend is not found in the UDF data. Indeed, the vast majority of our SFGs have Sérsic indices  $n \lesssim 1$ , thus they have not undergone the morphological transformation related to bulge formation. This indicates that the kinematical transformation (from high  $V/\sigma_t$  to low  $V/\sigma_t$ ) occurs before the morphological transformation toward bulge formation.

This scenario of kinematical transformation toward low  $j$  with smaller sizes<sup>13</sup> and larger dispersions is in agreement with the recent finding from the CANDELS survey (Osborne et al. 2020) that SFGs contains  $\sim 15\%$  of compact objects (‘blue nuggets’), indicating that compaction precedes quenching.

In local galaxies, Oh et al. (2020) separated the bulge and disk (stellar) kinematics of galaxies in the SAMI sample and found that the bulge (disk) component have low (high)  $V/\sigma$ , and follows the Faber-Jackson (Tully-Fisher) relation, respectively. We hypothesize that our  $0.4 < z < 1.4$  SFGs are their progeni-

tors, and  $z = 1$  SFGs with low  $V/\sigma$  will evolve into bulge dominated systems at  $z = 0$ . This is consistent with the TNG results of Tacchella et al. (2019), who found that the morphology of galaxies is set during their star-forming phase.

We return to Eq. (8) to gain insight on our results and in particular to address whether our relatively broad sAM sequence is consistent with the expected distribution of halo spins  $\lambda$ . One might expect the distribution of halo spins to be reflected in the scatter of the sAM sequence if each SFG retains a similar amount of sAM (a constant  $f_j = 1$ ), as in semi-analytical models. However, in hydro-dynamical simulations the situation is more complex (Genel et al. 2015; Jiang et al. 2019) given the potential large AM exchanges.

Figure 13 shows the normalization of Eq. (8), namely  $\log \tilde{j}_\star - f(\log M_\star) - a \log(1+z)$ , as a function of  $V/\sigma$  (corrected again to  $z = 1$ ) for the MUSE sample (left) and for the TNG50 sample (right), respectively. The left y-axis is found from the ‘fiducial’ fits shown in Figs. 11 and 12, which are listed in Table 1. The histograms in Fig. 13 show the distributions of Eq. (8) recast as  $\lambda f_j$  (right y-axis). For comparison, the solid line shows the log-normal distribution  $P(\lambda)$  expected for dark-matter halos (Bett et al. 2007) assuming a retention factor  $f_j$  of unity.

This figure shows that the distribution of SFGs in sAM is consistent with the expectation from dark-matter halos in TNG50, but is broader in our observations. The trend with  $V/\sigma$  is a strong function of galaxy sizes (SFR-weighted) in TNG50, but not in the MUSE sample. Another difference is the paucity of dispersion dominated galaxies in TNG50 (with 15% having  $V/\sigma < 3$ ) compared to the MUSE sample (with 50% having  $V/\sigma < 3$ ). Interestingly, the MUSE sample restricted to

<sup>13</sup> In this context, we note that our SFGs with low  $V/\sigma_t$  also tend to be smaller (as discussed below).

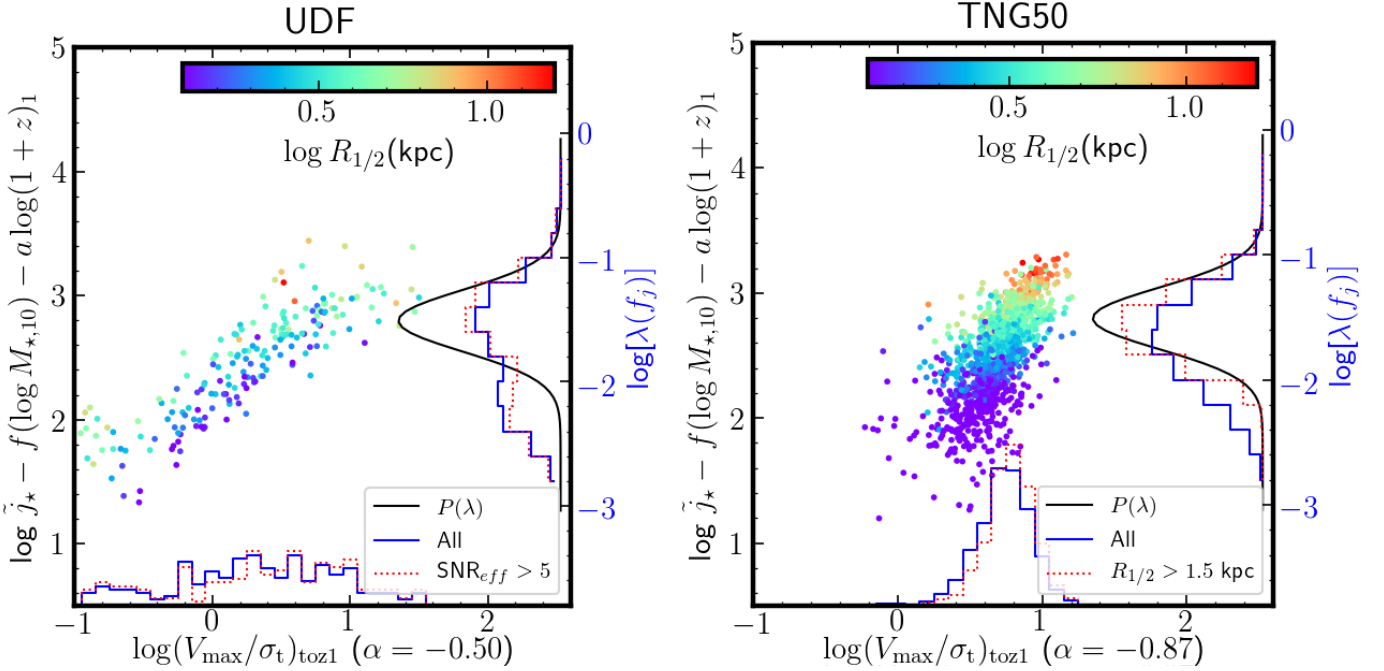


**Fig. 13.** *Left:* sAM sequence normalization as a function of  $(V/\sigma_t)_{\text{toz1}}$  for the UDF mosaic sample of SFGs where the color represents the SFR-weighted  $\log R_{1/2, [\text{O II}]}$ . The left y-axis  $\log \tilde{j}_* - f(\log M_*) - a \log(1+z)$  is found from the fiducial fits shown in Figs. 11–12 (see Table 1). The right y-axis shows the corresponding effective spin  $\lambda \times f_j$  according to Eq. (8) using the zero-pointing of Eq. (8). The solid histograms show the distributions from the data. The solid line shows the log-normal distribution  $P(\lambda)$  expected for halos (Bett et al. 2007). *Right:* same for the matched TNG50 sample of SFGs.

$S/N_{\text{eff}} > 5$  appears to show a more bimodal distributions in  $\lambda f_j$ , consistent with the  $z = 0$  RF12 results where rotation dominated galaxies have retained most of their halo sAM, while dispersion dominated systems have lost around 80% of their sAM.

## 7. Conclusions

The main purpose of this paper was to develop a robust methodology to measure  $j_{\text{tot}}$  from the angular momentum profiles  $j(<r)$  of galaxies in the low-mass regime (down to  $M_* = 10^8 M_\odot$ ), even when one is severely limited by S/N, surface-brightness limits and/or by the spatial resolution of ground-based instruments. The methodology consists of a two-step process (Sect. 2.3) and is based on the fitting algorithm GAIPAK<sup>3D</sup> (Bouché et al. 2015). The algorithm adjusts the morphological and dynamical parameters of a 3-dimensional disk model against the IFU data directly.

Using mock observations of SFGs taken from the TNG50 simulations (Nelson et al. 2019; Pillepich et al. 2019) with  $M_* = 10^{8.5-10.5} M_\odot$ , we have shown that our 3D methodology is able to recover the angular momentum profiles of SFGs with little bias ( $<5\%$ ) (Fig. 6) provided the S/N and/or surface brightness is sufficient (see Sect. 3.4). In particular, we find that we are able to estimate the  $j$  profiles of low-mass SFGs down to  $10^8 M_\odot$  with correspondingly small sizes. Specifically, galaxies must have  $S/N_{\text{eff}} \gtrsim 3$ , where  $S/N_{\text{eff}} = S/N_{\text{max}} (R_e/R_{\text{psf}})$  and  $S/N_{\text{max}}$  is the S/N in the brightest pixel,  $R_e$  is the half-light radius and  $R_{\text{psf}}$  is the PSF radius.

Using our 3D methodology on a sample of 182 SFGs (selected solely from their [O II] emission) with  $M_* > 10^8 M_\odot$  at  $0.4 < z < 1.5$  from the 9 arcmin<sup>2</sup> MUSE observations of Bacon et al. (2017), we have found the following:

- Our methodology allows us to determine galaxy sizes of unresolved SFGs with down to  $R_{1/2, [\text{O II}]} \approx 1$  kpc or  $0.2''$  (Fig. 10)

thanks to the built-in use of the PSF in our modeling. This opens a new parameter space (Fig. 10, right) between  $1 < R_e < 3$  kpc (and  $10^8 < M_* < 10^{9.5} M_\odot$ ) unexplored so far with IFS surveys beyond the local universe (e.g., Burkert et al. 2016; Swinbank et al. 2017; Harrison et al. 2017).

- We find that the  $\tilde{j}_* - M_*$  relation for SFGs is a nonlinear relation (Fig. 11, left) with  $\tilde{j}_* \propto M_*^{0.3-0.4}$  at  $M_* < 10^{9.5} M_\odot$  and  $\tilde{j}_* \propto M_*^{0.6}$  at  $M_* > 10^{9.5} M_\odot$ , similarly to RF12. This quadratic  $j - M$  relation appears to follow the expectations from simple disk formation models with the observed stellar mass fractions  $f_m$  (Moster et al. 2010; Behroozi et al. 2013). The zero-point of the sAM sequence at  $z = 1$  is found to be  $\log \tilde{j}_* = 2.85 \pm 0.05$  for rotation dominated  $\log M_* = 10$  SFGs both in the UDF and TNG50 samples.

- The  $\tilde{j}_* - M_*$  relation is a strong function of the dynamical status of SFGs quantified by  $V/\sigma_t$ , leading to a  $\tilde{j}_* - M_* - (V/\sigma)$  sequence (Fig. 11, right), where rotation dominated SFGs (with  $V/\sigma_t > 1-5$ ) follow the  $j - M$  relation of local disks, while dispersion dominated galaxies (with  $V/\sigma_t = 0.1$ ) follow the  $j - M$  relation of early types. This confirms the preliminary results of Contini et al. (2016) on a small sample and extends the results of Burkert et al. (2016) to the relatively unexplored regime below  $10^{10} M_\odot$  down to  $10^8 M_\odot$ .

- This  $j - M - (V/\sigma_t)$  relation is reminiscent of the  $z = 0$  results where the  $j - M$  relation is found to be a function of the bulge-to-total B/T ratio in local galaxies (e.g., Obreschkow & Glazebrook 2014; Fall & Romanowsky 2018) and is in relatively good qualitative agreement with theoretical framework on AM loss increasing with B/T in the EAGLE simulations (Zavala et al. 2016; Lagos et al. 2017) and with the results of Genel et al. (2015) from the Illustris simulations. Consequently, SFGs experience a dynamical transformation (from the disk to early type sequence of the  $j - M$  relation) and lower their sAMs prior to becoming passive, on the early-type  $j - M$  sequence.



– The ZP of the  $j - M - (V/\sigma_t)$  relation in the UDF sample (Fig. 11, right) evolves as  $\propto(1+z)^a$  with  $a = -0.27^{+0.42}_{-0.56}$  ( $2\sigma$ ), which is consistent with the expectation of  $(1+z)^{-0.5}$ , when taking into account the redshift evolution of  $V/\sigma_t$  ( $\propto(1+z)^{-0.5}$ ) for our definition of  $\sigma_t = \sigma(2R_e)$ .

– The ZP of the  $j - M - (V/\sigma_t)$  relation in the TNG50 sample (Fig. 12, right) evolves as  $\propto(1+z)^{-0.45\pm 0.25}$ , which is consistent with the expectation of  $(1+z)^{-0.5}$ , after taking into account the redshift evolution of  $V/\sigma_t$ , which goes as  $\propto(1+z)^{-0.85}$  for our definition of  $\sigma_t = \sigma(2R_e)$ . The  $j - M$  relation in the TNG50 sample is steeper with  $V/\sigma_t$ . This is likely to a combination of the difficulty in measuring  $\sigma_t$  in observations down to  $10 \text{ km s}^{-1}$  and to the physics detail in TNG50.

– The galaxy  $\lambda$  spin parameters (from the scatter of the  $j - M - (V/\sigma)$  relation) is broader in the MUSE sample than in TNG50 (Fig. 13), and also correlates better with galaxy sizes (SFR-weighted) in TNG50 than in the UDF observations.

– The MUSE sample restricted to  $S/N_{\text{eff}} > 5$  appears (Fig. 13, left) to show a more bimodal distributions in sAM, consistent with the  $z = 0$  RF12 results where rotation dominated galaxies have retained most of their halo sAM, while dispersion dominated systems have lost around 80% of their sAM.

We have shown that both in the UDF MUSE mosaic and in TNG50, SFGs follow a  $j - M - (V/\sigma)$  fundamental relation, and have highlighted the importance of taking into account the redshift evolution of  $V/\sigma$  in the redshift evolution of the sAM sequence  $j - M$ .

Our results demonstrate that it is possible to study the kinematics of large samples of SFGs blindly (i.e., without preselection on morphology, nor prior *HST* continuum detection) with little biases including the low-S/N regime of 3–5. Our 3D modeling technique opens the low-mass regime,  $M_\star < 10^9 M_\odot$ , at intermediate redshifts  $0.5 < z < 1.5$ , which had been unexplored so far.

*Acknowledgements.* This work made use of the following open source software: matplotlib (Hunter 2007), NumPy (Van Der Walt et al. 2011), SciPy (Jones et al. 2001), Astropy (Astropy Collaboration 2018). We thank the referee for his/her constructive comments that improved the quality of the paper. We thank L. Posti for insightful discussions that led to an improved manuscript. This study is based on observations collected at the European Southern Observatory under ESO programs 097.A-0138(A), 097.A-0144(A), 0100.A-0089(A). This work has been carried out thanks to the support of the ANR 3DGas-Flows (ANR-17-CE31-0017), the OCEVU Labex (ANR-11-LABX-0060). B. E. acknowledges financial support from the program National Cosmology et Galaxies (PNCG) of CNRS/INSU with INP and IN2P3, cofunded by CEA and CNES. R. B. acknowledges support from the ERC advanced grant 339659-MUSICOS. S. G., through the Flatiron Institute, is supported by the Simons Foundation. The primary TNG simulations were realized with compute time granted by the Gauss Centre for Super-computing (GCS): TNG50 under GCS Large-Scale Project GCS-DWAR (2016; PIs Nelson/Pillepich), and TNG100 and TNG300 under GCS-ILLU (2014; PI Springel) on the GCS share of the supercomputer Hazel Hen at the High Performance Computing Center Stuttgart (HLRS). GCS is the alliance of the three national supercomputing centres HLRS (Universität Stuttgart), JSC (Forschungszentrum Jülich), and LRZ (Bayerische Akademie der Wissenschaften), funded by the German Federal Ministry of Education and Research (BMBF) and the German State Ministries for Research of Baden-Württemberg (MWK), Bayern (StMWFK) and Nordrhein-Westfalen (MIWF).

## References

Abril-Melgarejo, V., Epinat, B., Mercier, W., et al. 2021, *A&A*, 647, A152  
 Alcorn, L. Y., Tran, K.-V., Glazebrook, K., et al. 2018, *ApJ*, 858, 47  
 Astropy Collaboration (Price-Whelan, A. M., et al.) 2018, *AJ*, 156, 123  
 Bacchini, C., Fraternali, F., Iorio, G., & Pezzulli, G. 2019, *A&A*, 622, A64  
 Bacon, R., Accardo, M., Adjali, L., et al. 2010, in *Society of Photo-Optical Instrumentation Engineers (SPIE) Conference Series*, SPIE Conf. Ser., 7735, 8  
 Bacon, R., Conseil, S., Mary, D., et al. 2017, *A&A*, 608, A1

Barcos, X., Lanzetta, K. M., & Webb, J. K. 1995, *Nature*, 376, 321  
 Behroozi, P. S., Wechsler, R. H., & Conroy, C. 2013, *ApJ*, 770, 57  
 Bett, P., Eke, V., Frenk, C. S., et al. 2007, *MNRAS*, 376, 215  
 Bett, P., Eke, V., Frenk, C. S., Jenkins, A., & Okamoto, T. 2010, *MNRAS*, 404, 1137  
 Bezanson, R., van der Wel, A., Pacifici, C., et al. 2018, *ApJ*, 858, 60  
 Boogaard, L. A., Brinchmann, J., Bouché, N., et al. 2018, *A&A*, 619, A27  
 Bouché, N., Cresci, G., Davies, R., et al. 2007, *ApJ*, 671, 303  
 Bouché, N., Murphy, M. T., Kacprzak, G. G., et al. 2013, *Science*, 341, 50  
 Bouché, N., Carfantan, H., Schroetter, I., Michel-Dansac, L., & Contini, T. 2015, *AJ*, 150, 92  
 Bouché, N., Finley, H., Schroetter, I., et al. 2016, *ApJ*, 820, 121  
 Bryan, G. L., & Norman, M. L. 1998, *ApJ*, 495, 80  
 Burkert, A., Genzel, R., Bouché, N., et al. 2010, *ApJ*, 725, 2324  
 Burkert, A., Förster Schreiber, N. M., Genzel, R., et al. 2016, *ApJ*, 826, 214  
 Butler, K. M., Obreschkow, D., & Oh, S.-H. 2017, *ApJ*, 834, L4  
 Catinella, B., Giovanelli, R., & Haynes, M. P. 2006, *ApJ*, 640, 751  
 Ceverino, D., Primack, J., Dekel, A., & Kassin, S. A. 2017, *MNRAS*, 467, 2664  
 Chabrier, G. 2003, *PASP*, 115, 763  
 Cole, J., Bezanson, R., van der Wel, A., et al. 2020, *ApJ*, 890, L25  
 Contini, T., Epinat, B., Bouché, N., et al. 2016, *A&A*, 591, A49  
 Cortese, L., Fogarty, L. M. R., Bekki, K., et al. 2016, *MNRAS*, 463, 170  
 Cresci, G., Hicks, E. K. S., Genzel, R., et al. 2009, *ApJ*, 697, 115  
 Daddi, E., Elbaz, D., Walter, F., et al. 2010, *ApJ*, 714, L118  
 Dalcanton, J. J., & Stilp, A. M. 2010, *ApJ*, 721, 547  
 Dalcanton, J. J., Spergel, D. N., & Summers, F. J. 1997, *ApJ*, 482, 659  
 Danovich, M., Dekel, A., Hahn, O., Ceverino, D., & Primack, J. 2015, *MNRAS*, 449, 2087  
 Davies, R., Förster Schreiber, N. M., Cresci, G., et al. 2011, *ApJ*, 741, 69  
 DeFelippis, D., Genel, S., Bryan, G. L., & Fall, S. M. 2017, *ApJ*, 841, 16  
 DeFelippis, D., Genel, S., Bryan, G. L., et al. 2020, *ApJ*, 895, 17  
 DeFelippis, D., Bouché, N.F., Genel, S., et al. 2021, *ApJ*, submitted, [arXiv:2102.08383]  
 Di Teodoro, E. M., & Fraternali, F. 2015, *MNRAS*, 451, 3021  
 Di Teodoro, E. M., Fraternali, F., & Miller, S. H. 2016, *A&A*, 594, A77  
 Dutton, A. A., & van den Bosch, F. C. 2009, *MNRAS*, 396, 141  
 Dutton, A. A., van den Bosch, F. C., & Dekel, A. 2010, *MNRAS*, 405, 1690  
 Efstathiou, G., & Jones, B. J. T. 1979, *MNRAS*, 186, 133  
 El-Badry, K., Quataert, E., Wetzel, A., et al. 2018, *MNRAS*, 473, 1930  
 Emsellem, E., Cappellari, M., Krajnović, D., et al. 2007, *MNRAS*, 379, 401  
 Epinat, B., Tasca, L., Amram, P., et al. 2012, *A&A*, 539, A92  
 Fall, S. M. 1983, *IAU*, 100, 391  
 Fall, S. M., & Efstathiou, G. 1980, *MNRAS*, 193, 189  
 Fall, S. M., & Romanowsky, A. J. 2013, *ApJ*, 769, L26  
 Fall, S. M., & Romanowsky, A. J. 2018, *ApJ*, 868, 133  
 Foreman-Mackey, D., Hogg, D. W., Lang, D., & Goodman, J. 2013, *PASP*, 125, 306  
 Förster Schreiber, N. M., Genzel, R., Lehnert, M. D., et al. 2006, *ApJ*, 645, 1062  
 Genel, S., Vogelsberger, M., Springel, V., et al. 2014, *MNRAS*, 445, 175  
 Genel, S., Fall, S. M., Hernquist, L., et al. 2015, *ApJ*, 804, L40  
 Genel, S., Nelson, D., Pillepich, A., et al. 2018, *MNRAS*, 474, 3976  
 Genzel, R., Burkert, A., Bouché, N., et al. 2008, *ApJ*, 687, 59  
 Genzel, R., Tacconi, L. J., Gracia-Carpio, J., et al. 2010, *MNRAS*, 407, 2091  
 Genzel, R., Schreiber, N. M. F., Übler, H., et al. 2017, *Nature*, 543, 397  
 Genzel, R., Price, S. H., Übler, H., et al. 2020, *ApJ*, 902, 98  
 Geweke, J. 1992, in *Bayesian Statistics* (University Press), 169  
 Gillman, S., Tiley, A. L., Swinbank, A. M., et al. 2020, *MNRAS*, 492, 1492  
 Graham, A. W., Driver, S. P., Petrosian, V., et al. 2005, *AJ*, 130, 1535  
 Grand, R. J. J., van de Voort, F., Zjupa, J., et al. 2019, *MNRAS*, 490, 4786  
 Guérou, A., Krajnović, D., Epinat, B., et al. 2017, *A&A*, 608, A5  
 Harrison, C. M., Johnson, H. L., Swinbank, A. M., et al. 2017, *MNRAS*, 467, 1965  
 Ho, S. H., Martin, C. L., Kacprzak, G. G., & Churchill, C. W. 2017, *ApJ*, 835, 267  
 Ho, S. H., Martin, C. L., & Turner, M. L. 2019, *ApJ*, 875, 54  
 Hunter, J. D. 2007, *Comput. Sci. Eng.*, 9, 90  
 Inami, H., Bacon, R., Brinchmann, J., et al. 2017, *A&A*, 608, A2  
 Jiang, F., Dekel, A., Kneller, O., et al. 2019, *MNRAS*, 488, 4801  
 Jones, E., Oliphant, T., Peterson, P., et al. 2001, *SciPy: Open Source Scientific Tools for Python*  
 Kassin, S. A., Weiner, B. J., Faber, S. M., et al. 2007, *ApJ*, 660, L35  
 Kassin, S. A., Weiner, B. J., Faber, S. M., et al. 2012, *ApJ*, 758, 106  
 Kennicutt, R. C. 1998, *ARA&A*, 36, 189  
 Kretschmer, M., Agertz, O., & Teyssier, R. 2020, *MNRAS*, 497, 4346  
 Kriek, M., van Dokkum, P. G., Franx, M., Illingworth, G. D., & Magee, D. K. 2009, *ApJ*, 705, L71  
 Lagos, C., Theuns, T., Stevens, A. R. H., et al. 2017, *MNRAS*, 3870, 3850  
 Lang, P., Meidt, S. E., Rosolowsky, E., et al. 2020, *ApJ*, 897, 122

- Lapi, A., Salucci, P., & Danese, L. 2018, *ApJ*, 859, 2
- Leroy, A. K., Walter, F., Brinks, E., et al. 2008, *AJ*, 136, 2782
- Li, J., Obreschkow, D., Lagos, C., et al. 2020, *MNRAS*, 493, 5024
- Lopez, S., Tejos, N., Ledoux, C., et al. 2018, *Nature*, 554, 493
- Macciò, A. V., Dutton, A. A., van den Bosch, F. C., et al. 2007, *MNRAS*, 378, 55
- Mancera Piña, P. E., Posti, L., Fraternali, F., Adams, E. A. K., & Oosterloo, T. 2021, *A&A*, 647, A76
- Marasco, A., Fraternali, F., Posti, L., et al. 2019, *A&A*, 621, L6
- Marinacci, F., Vogelsberger, M., Pakmor, R., et al. 2018, *MNRAS*, 480, 5113
- Martin, C. L., Ho, S. H., Kacprzak, G. G., & Churchill, C. W. 2019, *ApJ*, 878, 84
- Martinsson, T. P. K., Verheijen, M. A. W., Westfall, K. B., et al. 2013, *A&A*, 557, A130
- Meurer, G. R., Carignan, C., Beaulieu, S. F., & Freeman, K. C. 1996, *AJ*, 111, 1551
- Mitchell, P. D., Lacey, C. G., Lagos, C. D. P., et al. 2018, *MNRAS*, 474, 492
- Mo, H. J., Mao, S., & White, S. D. M. 1998, *MNRAS*, 295, 319
- Moster, B. P., Somerville, R. S., Maulbetsch, C., et al. 2010, *ApJ*, 710, 903
- Mowla, L., van der Wel, A., van Dokkum, P., & Miller, T. B. 2019, *ApJ*, 872, L13
- Murugesan, C., Kilborn, V., Jarrett, T., et al. 2020, *MNRAS*, 496, 2516
- Naiman, J. P., Pillepich, A., Springel, V., et al. 2018, *MNRAS*, 477, 1206
- Navarro, J. F., & Steinmetz, M. 2000, *ApJ*, 538, 477
- Nelson, E. J., van Dokkum, P. G., Förster Schreiber, N. M., et al. 2016, *ApJ*, 828, 27
- Nelson, D., Pillepich, A., Springel, V., et al. 2018, *MNRAS*, 475, 624
- Nelson, D., Pillepich, A., Springel, V., et al. 2019, *MNRAS*, 490, 3234
- Obreschkow, D., & Glazebrook, K. 2014, *ApJ*, 784, 26
- Obreschkow, D., Glazebrook, K., Bassett, R., et al. 2015, *ApJ*, 815, 97
- Obreschkow, D., Glazebrook, K., Kilborn, V., & Lutz, K. 2016, *ApJ*, 824, L26
- Oh, S., Colless, M., Barsanti, S., et al. 2020, *MNRAS*, 495, 4638
- Osborne, C., Salim, S., Damjanov, I., et al. 2020, *ApJ*, 902, 77
- Peebles, P. J. E. 1969, *ApJ*, 155, 393
- Persic, M., Salucci, P., & Stel, F. 1996, *MNRAS*, 281, 27
- Pillepich, A., Nelson, D., Hernquist, L., et al. 2018a, *MNRAS*, 475, 648
- Pillepich, A., Springel, V., Nelson, D., et al. 2018b, *MNRAS*, 473, 4077
- Pillepich, A., Nelson, D., Springel, V., et al. 2019, *MNRAS*, 490, 3196
- Planck Collaboration XIII. 2016, *A&A*, 594, A13
- Posti, L., Pezzulli, G., Fraternali, F., & Di Teodoro, E. M. 2018a, *MNRAS*, 475, 232
- Posti, L., Fraternali, F., Di Teodoro, E. M., & Pezzulli, G. 2018b, *A&A*, 612, L6
- Posti, L., Marasco, A., Fraternali, F., & Famaey, B. 2019, *A&A*, 629, A59
- Prugniel, P., & Simien, F. 1997, *A&A*, 321, 111
- Refregier, A., Kacprzak, T., Amara, A., Bridle, S., & Rowe, B. 2012, *MNRAS*, 425, 1951
- Renzini, A. 2020, *MNRAS*, 495, L42
- Rizzo, F., Fraternali, F., & Iorio, G. 2018, *MNRAS*, 476, 2137
- Romanowsky, A. J., & Fall, S. M. 2012, *ApJS*, 203, 17
- Romeo, A. B. 2020, *MNRAS*, 491, 4843
- Romeo, A. B., & Mogotsi, K. M. 2018, *MNRAS*, 480, L23
- Salvatier, J., Wiecki, T. V., & Fonnesbeck, C. 2016, *PeerJ Comput. Sci.*, 2
- Schaye, J., Crain, R. A., Bower, R. G., et al. 2015, *MNRAS*, 446, 521
- Sérsic, J. L. 1963, *Boletín de la Asociacion Argentina de Astronomia La Plata Argentina*, 6, 41
- Sharma, S., Steinmetz, M., & Bland-Hawthorn, J. 2012, *ApJ*, 750, 107
- Sharples, R., Bender, R., Agudo Berbel, A., et al. 2013, *Messenger*, 151, 21
- Somerville, R. S., Behroozi, P., Pandya, V., et al. 2018, *MNRAS*, 473, 2714
- Springel, V. 2010, *MNRAS*, 401, 791
- Springel, V., & Hernquist, L. 2003, *MNRAS*, 339, 312
- Springel, V., Pakmor, R., Pillepich, A., et al. 2018, *MNRAS*, 475, 676
- Steidel, C. C., Kollmeier, J. A., Shapley, A. E., et al. 2002, *ApJ*, 570, 526
- Stevens, A. R. H., Croton, D. J., & Mutch, S. J. 2016, *MNRAS*, 461, 859
- Stewart, K. R., Brooks, A. M., Bullock, J. S., et al. 2013, *ApJ*, 769, 74
- Stewart, K. R., Maller, A. H., Oñorbe, J., et al. 2017, *ApJ*, 843, 47
- Stott, J. P., Swinbank, A. M., Johnson, H. L., et al. 2016, *MNRAS*, 457, 1888
- Straatman, C. M. S., Glazebrook, K., Kacprzak, G. G., et al. 2017, *ApJ*, 839, 57
- Sweet, S. M., Fisher, D., Glazebrook, K., et al. 2018, *ApJ*, 860, 37
- Swinbank, A. M., Harrison, C. M., Trayford, J., et al. 2017, *MNRAS*, 467, 3140
- Tacchella, S., Diemer, B., Hernquist, L., et al. 2019, *MNRAS*, 487, 5416
- Teklu, A. F., Remus, R.-S., Dolag, K., et al. 2015, *ApJ*, 812, 29
- Tiley, A. L., Bureau, M., Cortese, L., et al. 2019, *MNRAS*, 482, 2166
- Übler, H., Förster Schreiber, N. M., Genzel, R., et al. 2017, *ApJ*, 842, 121
- Übler, H., Genzel, R., Wisnioski, E., et al. 2019, *ApJ*, 880, 48
- van den Bosch, F. C., Abel, T., & Hernquist, L. 2003, *MNRAS*, 346, 177
- Van Der Walt, S., Colbert, S. C., & Varoquaux, G. 2011, *Comput. Sci. Eng.*, 13, 22
- van der Wel, A., Chang, Y.-Y., Bell, E. F., et al. 2014, *ApJ*, 792, L6
- van de Sande, J., Kriek, M., Franx, M., et al. 2013, *ApJ*, 771, 85
- Vogelsberger, M., Sijacki, D., Kereš, D., Springel, V., & Hernquist, L. 2012, *MNRAS*, 425, 3024
- Vogelsberger, M., Genel, S., Sijacki, D., et al. 2013, *MNRAS*, 436, 3031
- Vogelsberger, M., Genel, S., Springel, V., et al. 2014a, *Nature*, 509, 177
- Vogelsberger, M., Genel, S., Springel, V., et al. 2014b, *MNRAS*, 444, 1518
- Vogelsberger, M., Marinacci, F., Torrey, P., & Puchwein, E. 2020, *Nat. Rev. Phys.*, 2, 42
- Weinberger, R., Springel, V., Hernquist, L., et al. 2017, *MNRAS*, 465, 3291
- Whitaker, K. E., Franx, M., Leja, J., et al. 2014, *ApJ*, 795, 104
- White, S. D. M., & Rees, M. J. 1978, *MNRAS*, 183, 341
- Wilman, D. J., Fossati, M., Mendel, J. T., et al. 2020, *ApJ*, 892, 1
- Wisnioski, E., Förster Schreiber, N. M., Wuyts, S., et al. 2015, *ApJ*, 799, 209
- Wisnioski, E., Förster Schreiber, N. M., Fossati, M., et al. 2019, *ApJ*, 886, 124
- Zabl, J., Bouché, N. F., Schroetter, I., et al. 2019, *MNRAS*, 485, 1961
- Zavala, J., Frenk, C. S., Bower, R., et al. 2016, *MNRAS*, 460, 4466

## Appendix A: Analytical derivation

For a Sérsic profile  $I(r) \propto \exp[-b_n (R/R_e)^{1/n}]$ , we can calculate the coefficient  $k_n$  in Eq. (3) assuming a constant flat rotation curve such as  $V(R) = V_c$  as in RF12. Using Eq. (2) and by substituting by  $x = b_n \left(\frac{R}{R_e}\right)^{1/n}$ , we find

$$j_t = V_c \frac{\int dR R^2 e^{-b_n \left(\frac{R}{R_e}\right)^{1/n}}}{\int dR R e^{-b_n \left(\frac{R}{R_e}\right)^{1/n}}}, \quad (\text{A.1})$$

$$= V_c \frac{n \frac{R_e^3}{b_n^3} \Gamma(3n)}{n \frac{R_e^2}{b_n^2} \Gamma(2n)}, \quad (\text{A.2})$$

$$= V_c R_e \frac{1}{b_n} \frac{\Gamma(3n)}{\Gamma(2n)}, \quad (\text{A.3})$$

which means that the  $k_n$  coefficient in Eq. (3) is

$$k_n = \frac{1}{b_n} \frac{\Gamma(3n)}{\Gamma(2n)}. \quad (\text{A.4})$$

where  $\Gamma$  is the gamma function. As discussed in [Graham et al. \(2005\)](#), the Sérsic coefficient  $b_n$  is given from the solution of the following equation

$$\Gamma(2n) = 2 \gamma(2n, b_n) \quad (\text{A.5})$$

where  $\Gamma$  is the (complete) gamma function and  $\gamma$  is the incomplete gamma function. Note, the Sérsic coefficient  $b_n$  can be also approximated by  $b_n \approx 1.9992n - 0.327$  as discussed in [Graham et al. \(2005\)](#) (see also [Prugniel & Simien 1997](#)).

## Appendix B: Selection function

Due to the instrumental resolution of  $R \sim 3000$  ( $\sim 100 \text{ km s}^{-1}$  or  $\sim 50 \text{ km s}^{-1}$  per pixel) for MUSE, we are limited to a few tens of  $\text{km s}^{-1}$  in either  $V_{\text{max}}$  or  $\sigma_t$ . In order to quantify the impact of this limit to the  $j - M - (V/\sigma)$  relation,  $\log \tilde{j}_\star = f(\log M_\star) + \gamma \log(V_{\text{max}}/\sigma_t)$ , we assume a constant floor  $K$  for  $V_{\text{max}}^2 + \sigma_t^2$ , which becomes

$$K = r^2 (\sin^2(\theta) + \cos^2(\theta)) \quad (\text{B.1})$$

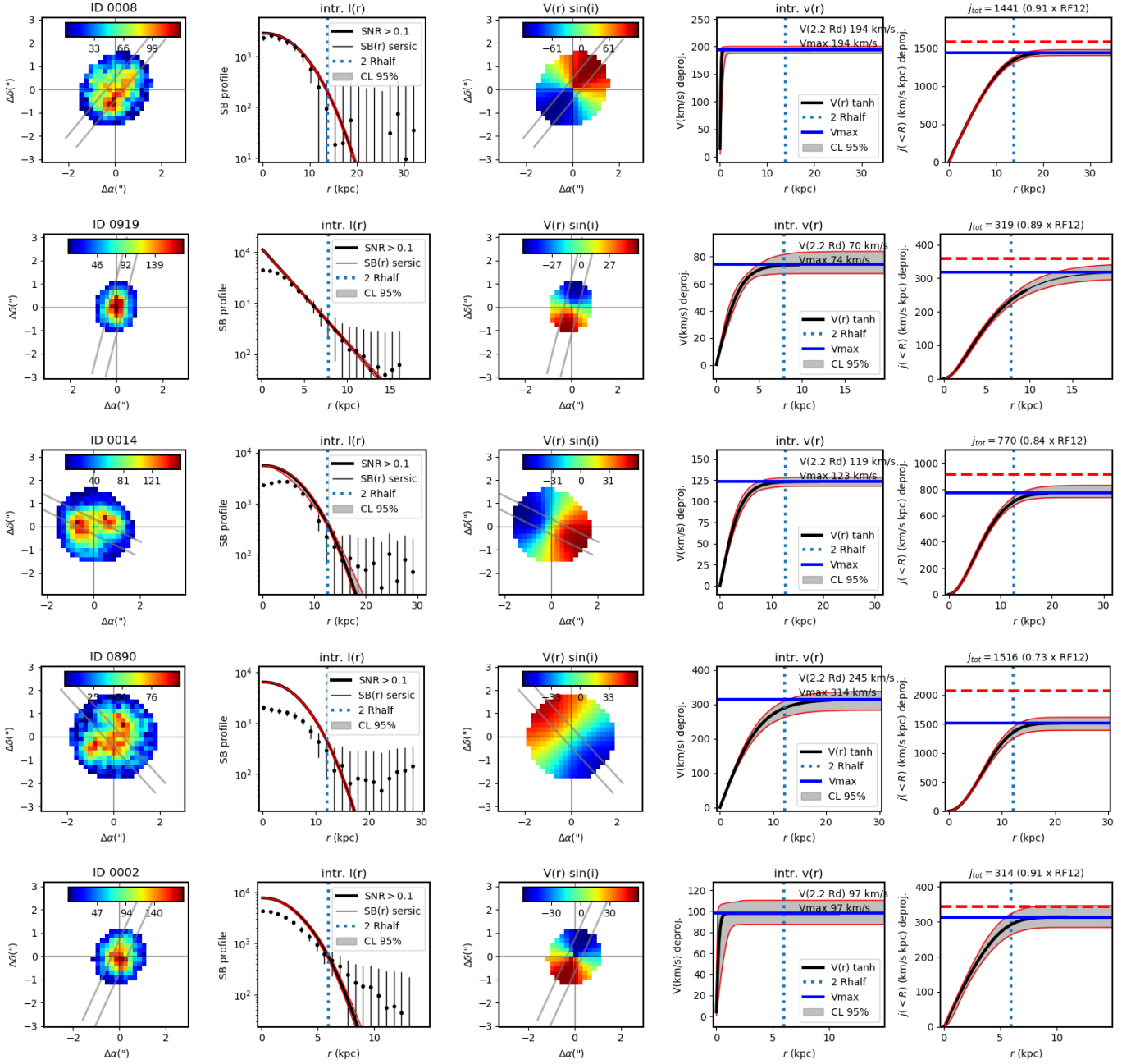
after a change of variables with  $\tan(\theta) = \frac{v}{\sigma_t}$  and  $|K| = r^2$ . This implies that the  $j - M - (V/\sigma)$  relation becomes

$$\log \tilde{j}_\star = f(\log M_\star) + \gamma \log(\tan(\theta)). \quad (\text{B.2})$$

Finally, the last term can be expressed as a function of  $M_\star$  using the  $S05 - M_\star$  relation (e.g., [Kassin et al. 2007](#); [Übler et al. 2017](#); [Tiley et al. 2019](#)), namely  $\log S05 \approx 0.3 \log M_{\star,9} + 1.5$ , and  $S_{05}^2 \equiv 0.5V_{\text{max}}^2 + \sigma_t^2 = r^2 [0.5 \sin^2(\theta) + \cos^2(\theta)]$ .

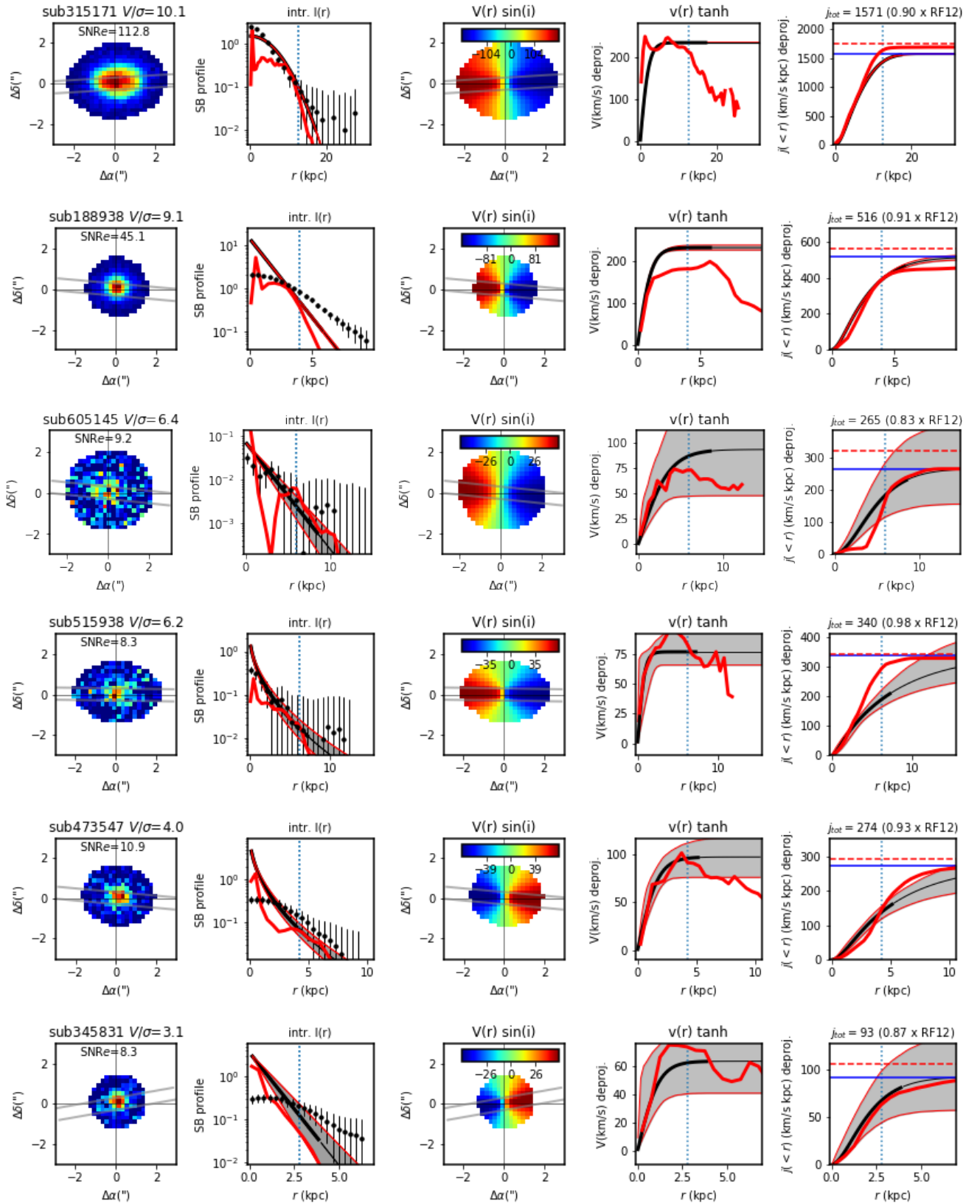
**Appendix C: Kinematics**

Fig. C.1 shows examples of kinematic properties for UDF mosaic galaxies analyzed in § 4.3.



**Fig. C.1.** Morphology and kinematics of examples from the UDF-mosaic sample. The panels show the flux map, the SB profile  $\Sigma_{\text{SFR}}$ , the velocity field, the rotation curve and the SFR-weighted  $j_*( < r)$  profiles, respectively. The 1D profiles are determined along the pseudo-long slits represented by the gray straight lines (black solid lines), along with the 95% confidence intervals. The vertical dotted lines represent  $2 \times R_e$ . In the last column, the horizontal blue lines show the total modeled angular momentum  $j_{3D}$ , while the horizontal red lines show the total  $j_*$  using the Eq. (3) approximation.

Fig. C.2 shows examples of kinematic properties for TNG50 galaxies analyzed in § 3.4.



**Fig. C.2.** Kinematic properties of some of the TNG50 galaxies. The panels show the flux map, the SB profile  $\Sigma_{\text{SFR}}$ , the velocity field, the rotation curve and the SFR-weighted  $\tilde{j}_*( < r)$  profiles, respectively. The 1D profiles are determined along the pseudo-long slits represented by the gray straight lines (black solid lines), along with the 95% confidence intervals. The vertical dotted lines represent  $2 \times R_c$ . The 1D red solid lines represent the true profile determined directly from the TNG50 data. In the last column, the horizontal blue lines show the total modeled angular momentum  $\tilde{j}_{3D}$ , while the horizontal red lines show the total  $\tilde{j}_*$  using the Eq. (3) formula. This approximation can lead to an over-estimation of the total angular momentum by 10–30% depending on the steepness of the  $v(r)$  profile.

### Appendix D: Redshift evolution of $V/\sigma$

In order to estimate the redshift evolution  $q$  of  $V/\sigma_t$ , we minimized the  $V/\sigma_t$  distribution with respect to  $q$ . Fig. D.1 shows the

results of this exercise for the TNG50 (UDF) sample in the left (right) panel, respectively. This figure shows that  $V/\sigma_t$  evolves as  $(1+z)^{-0.8}$  in TNG50 and as  $(1+z)^{-0.5}$  in the UDF sample.

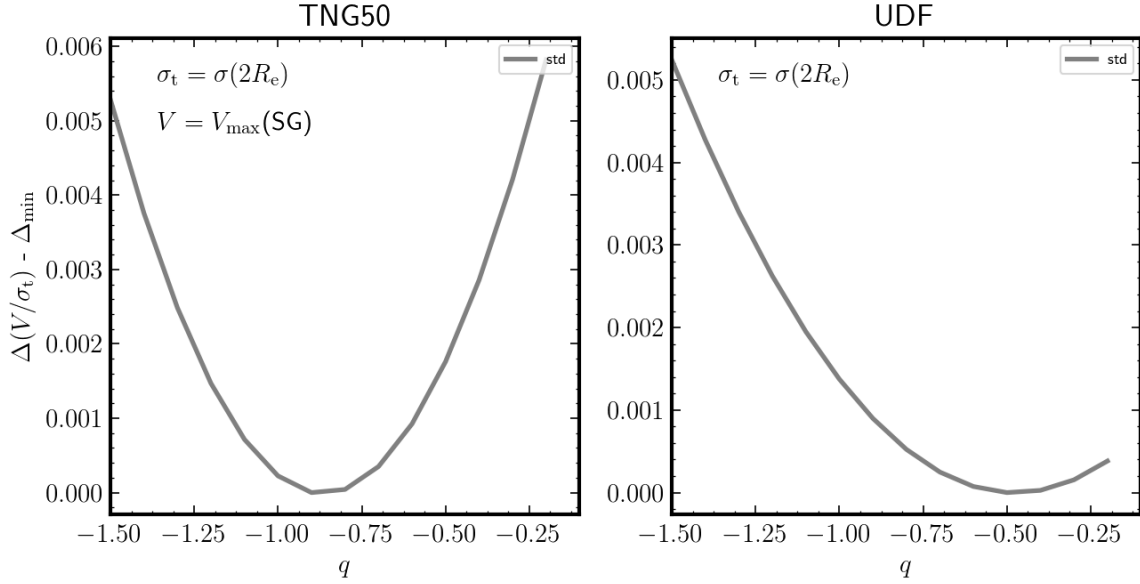


**Fig. D.1.** *Left:*  $V/\sigma$  standard distribution as a function of the redshift evolution  $q$  (Eq. (10)). One sees that  $q \sim -0.8$  minimizes the distribution across all redshifts. *Right:* Same for the UDF sample. The redshift evolution for  $V/\sigma$  here is  $q \approx -0.5$ .